Advances in Applied Mathematics and Mechanics
Adv. Appl. Math. Mech., Vol. **xx**, No. x, pp. 1-33

DOI: 10.4208/aamm.OA-2023-0107
xxx 2024

A Novel Construction of Distribution Function through Second-Order Polynomial Approximation in Terms of Particle Mass, Momentum and Energy

Z. Y. Yuan[1], Z. Chen[2], C. Shu[3,*], Y. Y. Liu[3] and Z. L. Zhang[4]

[1] *School of Energy and Power Engineering, Nanjing University of Science and Technology, Nanjing, Jiangsu 210094, China*
[2] *School of Naval Architecture, Ocean and Civil Engineering, Shanghai Jiao Tong University, Shanghai 200240, China*
[3] *Department of Mechanical Engineering, National University of Singapore, 10 Kent Ridge Crescent, 119260, Singapore*
[4] *Department of Mechanical and Process Engineering, ETH Zürich, Leonhardstrasse 21, Zürich 8092, Switzerland*

Received 19 April 2023; Accepted (in revised version) 3 July 2023

Abstract. In this paper, we propose a new way to construct the distribution function through the second-order polynomial approximation in terms of particle mass, momentum and energy. The new construction holds three distinguished features. First, the formulations are more concise as compared with the third-order truncated Hermite polynomial expansion which yields Grad's 13-moment distribution function; Second, all moments of the present distribution function are determined from conservation laws; Third, these moments are closely linked to the most desirable variables, such as mass, momentum and energy. Then, this new distribution function is applied to construct a new gas kinetic flux solver. Numerical validations show that the proposed method recovers the Navier-Stokes solutions in the continuum regime. In addition, it outperforms Grad's 13-moment distribution function in the transition regime, especially in the prediction of temperature and heat flux.

AMS subject classifications: 82C40

Key words: Second-order truncated expansion, peculiar velocity space, compatibility conditions and moment relationships, gas kinetic flux solver, continuum regime to rarefied regime.

1 Introduction

The classical Navier-Stokes (NS) equations have been widely utilized for the research of fluid mechanics. NS equations rely on the assumption of local thermodynamic equi-

*Corresponding author.
Email: mpeshuc@nus.edu.sg (C. Shu)

librium. However, this assumption is unjustifiable for systems beyond the continuum flow regime. For example, in the micromachining and micro-electromechanical system (MEMS), the micro-devices are usually in the scale of micrometers. Hence, the characteristic length is usually comparable with the molecular mean free path. In such scenario, the interactions between the molecules are insufficient and the assumption of thermodynamic equilibrium fails, so do the Navier-Stokes (NS) equations established on this assumption.

To describe the non-equilibrium processes, much attention has been put on more sophisticated models, such as kinetic theory and molecular dynamics, which are not constrained by the assumption of thermodynamic equilibrium. The Boltzmann equation is derived from the kinetic theory and physically interprets the collision and transport processes of gas molecules. Based on that, many numerical approaches have been proposed to solve the Boltzmann equation for academic explorations and engineering applications, among which one popular numerical method is the discrete velocity method (DVM). Various versions of DVM include gas kinetic unified algorithm [1, 2], unified gas kinetic scheme [3,4], discrete unified gas kinetic scheme [5,6] and so on. The essence of DVM is to evolve the distribution function of gas molecules, based on which the macroscopic flow variables can be calculated from the moments of the distribution function. However, the evolution of the gas distribution function calls for additional discretization in the particle velocity space, which consumes huge computational efforts and virtual memories.

To avoid the discretization in the velocity space, the explicit formulation of gas distribution function should be given. One common way to construct the gas distribution function is the first-order Chapman-Enskog (CE) expansion [7–11]. Some well-known solvers were proposed based on the CE expansion, such as lattice Boltzmann flux solver (LBFS) [12, 13], gas kinetic scheme (GKS) [14, 15], circular function-based gas kinetic scheme (C-GKS) [16,17], novel gas kinetic flux solver (N-GKFS) [18] and so on. However, the first-order CE expansion can only recover the Navier-Stokes (NS) equations, which constrains the applications of the aforementioned solvers to continuum flow regime at the thermodynamic equilibrium state. To solve flow problems beyond the NS level, a more general distribution function should be adopted. It is noteworthy that the second-order and the third-order CE expansions respectively yield the Burnett and the Supper-Burnett equations. To certain extent, the gas kinetic flux solvers based on these expansions can simulate flows beyond the NS level. However, the gas distribution function that satisfies the Burnett or the Supper-Burnett equations contains the second-order or the third-order spatial derivatives. The treatments of these high-order spatial derivatives complicate the solvers. To alleviate this issue, a variant of gas kinetic flux solver [19] was proposed, which includes the correction terms to the linearized constitutive relations and Fourier's law. The validation results showed that the correction terms indeed take effect in the non-equilibrium regime. However, the effectiveness of the correction terms will reduce with the increasing of the Knudsen numbers.

Another way to construct the gas distribution function is the Hermite polynomial expansion [20]. The regularized 13-moment method [21] and regularized 26-moment

method [22] were proposed based on this way. The success of regularized moment methods implies that the gas distribution function obtained through Hermite polynomial expansion has a potential for resolving flows beyond the NS level. Then, a novel solver [23,24] and a Grad's distribution function-based gas kinetic scheme [25] were proposed, which combines the advantages of the DVM and the moment method. On the one hand, these methods adopt the Grad's distribution function as the initial one and thus circumvent the tedious evolution process of gas distribution function in DVM. On the other hand, they calculate the high-order moments through the moment relationships and thus avoid solving additional partial differential equations in the moment methods. The validation results of the novel solver and the Grad's distribution function-based gas kinetic scheme show their effectiveness in simulating flows from the continuum regime to the rarefied regime at moderate Knudsen numbers.

A common pitfall of both the novel solver and the Grad's distribution function-based gas kinetic scheme is that their solution accuracy depends on the formulation of the initially guessed distribution function. In practice, the initial gas distribution function obtained from the Grad's 26 (fourth-order truncated Hermite polynomial expansion) performs better than Grad's 13 distribution function (the third-order truncation). This is within our expectations because with higher-order expansion terms involved, the approximated gas distribution function bears higher accuracy. However, a higher-order expansion is inevitably accompanied by more complicated formulations. At the same time, it is noted that the better performance of Grad's 26 distribution function is mainly presented in the prediction of velocity profiles rather than in the temperature profiles, which stems from the fact that the higher-order additional moments involved in the Grad's 26 distribution function are not closely related to the energy (or temperature). Observing these puzzles, a natural question is whether a distribution function, which is closely related to the energy, can be constructed.

The answer towards this question motivates the present work. From the perspective of gas kinetic theory, the most desirable macroscopic variables, such as density, momentum and energy can be calculated by moments of f, $\boldsymbol{\xi}\cdot f$ and $\frac{1}{2}\cdot\boldsymbol{\xi}^2\cdot f$, respectively. Here, f is the distribution function, $\boldsymbol{\xi}$ is the molecular velocity (summation of mean velocity $\boldsymbol{U}$ and peculiar velocity $\boldsymbol{C}$). From the Hermite polynomial expansion, it can be seen that the definitions of moments are all associated with the peculiar velocity $\boldsymbol{C}$. Hence, a natural way to construct moments that are closely linked to density, momentum and energy is to employ polynomial approximation in terms of $\mathbf{1}$, $\boldsymbol{C}$, $\boldsymbol{C}^{\mathbf{2}}$. In this paper, a second-order polynomial approximation in terms of $\mathbf{1}$, $\boldsymbol{C}$, $\boldsymbol{C}^{\mathbf{2}}$ is used to derive the distribution function. By utilizing the compatibility conditions and the moment relationships, all coefficients in the polynomial approximation can be determined and generally expressed as $\langle \boldsymbol{C}^m f\rangle$. And this distribution function will be adopted as the initially guessed distribution function to establish a new gas kinetic flux solver. Numerical validations show that this new gas kinetic flux solver is applicable to both the continuum flow regime and the transition flow regime. Comparing with the Grad's 13-based method, the present solver has more compact formulations and performs better in the prediction of temperature and

heat flux.

The organization of the rest of the paper is summarized as follows. In Section 2, the Boltzmann equation and the gas kinetic flux solver will be briefly introduced. In Section 3, the gas distribution obtained by the second-order polynomial approximation in terms of $\mathbf{1}$, $\boldsymbol{C}$, $\boldsymbol{C}^2$ will be shown. Section 4 gives the details of the present gas kinetic flux solver. In Section 5, numerical validations will be presented. Concluding remarks will be made in Section 6.

2 Brief description on Boltzmann equation and gas kinetic flux solver

2.1 Boltzmann equation

From the mesoscopic perspective, gas molecules exhibit transport and collision behaviors constantly. The Boltzmann equation is such an equation that physically interprets these processes by evolving the gas distribution function f. Its formulation with the Bhatnagar–Gross–Krook (BGK) collision model [26] can be given as,

$$\frac{\partial f}{\partial t}+\boldsymbol{\xi}\cdot\nabla f=\frac{g-f}{\tau}, \tag{2.1}$$

where t is the time and $\boldsymbol{\xi}=(\xi_1,\xi_2,\xi_3)$ represents the particle velocity space. τ is the relaxation time and defined as the ratio of the dynamic viscosity μ to the pressure p. g is the equilibrium state of the gas distribution function and can be expressed as,

$$g=\frac{\rho}{(2\pi RT)^{\frac{3}{2}}}\cdot\exp\left(-\frac{\boldsymbol{C}^2}{2RT}\right), \tag{2.2}$$

in which, ρ is the macroscopic density, $\boldsymbol{C}=(C_1,C_2,C_3)$ denotes the peculiar velocity and T is the macroscopic temperature. R is the gas constant.

2.2 Gas kinetic flux solver

From the macroscopic perspective, the desired flow variables including density, velocity and temperature correspond to different moments of the gas distribution function [27,28]. Hence, the Boltzmann equation shown in Eq. (2.1) can be projected to the macroscopic level by taking the relevant moments of gas distribution function. In other words, we can multiply Eq. (2.1) with the moment vector $\boldsymbol{\varphi}=(1,\boldsymbol{\xi},\boldsymbol{\xi}^2/2)$ and then integrate it over the whole velocity space. Finally, the formulation is obtained as follows,

$$\frac{\partial}{\partial t}\langle\boldsymbol{\varphi}f\rangle+\nabla\cdot\langle\boldsymbol{\varphi}\boldsymbol{\xi}f\rangle=\frac{\langle\boldsymbol{\varphi}(g-f)\rangle}{\tau}, \tag{2.3}$$

where the operator $\langle\cdots\rangle$ is the integration over the whole velocity space and can be expressed as

$$\langle\cdots\rangle=\int_{-\infty}^{+\infty}\int_{-\infty}^{+\infty}\int_{-\infty}^{+\infty}(\cdots)d\xi_1 d\xi_2 d\xi_3. \tag{2.4}$$

The moment relationships reveal that the terms $\langle\boldsymbol{\varphi}f\rangle$ and $\langle\boldsymbol{\varphi}\boldsymbol{\xi}f\rangle$ in Eq. (2.3) are equivalent to the macroscopic variables $\boldsymbol{W}=\left(\rho,\quad \rho\boldsymbol{U},\quad \rho E\right)$ and the flux vector $\boldsymbol{F}$, respectively. In the meantime, the compatibility condition means that $\langle\boldsymbol{\varphi}g\rangle$ and $\langle\boldsymbol{\varphi}f\rangle$ should recover the same macroscopic variables, which yields $\langle\boldsymbol{\varphi}(g-f)\rangle=0$. With these relationships, the macroscopic conservative equations can be obtained as

$$\frac{\partial\boldsymbol{W}}{\partial t}+\nabla\cdot\boldsymbol{F}=0. \tag{2.5}$$

Eq. (2.5) is a macroscopic equivalence of the mesoscopic governing equation (2.1). An important part to solve Eq. (2.5) is the accurate construction of numerical fluxes $\boldsymbol{F}$. The conventional computational fluid dynamics (CFD) method usually constructs the inviscid flux and viscous flux separately. However, the gas kinetic flux solver [29] (GKFS) can construct the numerical fluxes simultaneously. It constructs the numerical fluxes by taking the moment of gas distribution function at cell interface as $\boldsymbol{F}=\langle\boldsymbol{\varphi}\boldsymbol{\xi}f\rangle$.

To retain the kinetic feature, the distribution function at the cell interface can be physically derived through Boltzmann equation with BGK collision term, which has been shown in Eq. (2.1). By discretizing the Boltzmann equation within a time step δt and at the cell interface $\boldsymbol{x}_{I+\frac{1}{2}}$, we can obtain the formulation as follows,

$$\frac{f\left(\boldsymbol{x}_{I+\frac{1}{2}},\boldsymbol{\xi},t+\delta t\right)-f\left(\boldsymbol{x}_{I+\frac{1}{2}}-\boldsymbol{\xi}\delta t,\boldsymbol{\xi},t\right)}{\delta t}=\frac{g\left(\boldsymbol{x}_{I+\frac{1}{2}},\boldsymbol{\xi},t+\delta t\right)-f\left(\boldsymbol{x}_{I+\frac{1}{2}},\boldsymbol{\xi},t+\delta t\right)}{\tau}. \tag{2.6}$$

The left-hand side of Eq. (2.6) represents the discretization of substantial derivative of distribution function $\partial f/\partial t+\boldsymbol{\xi}\cdot\nabla f$. The right-hand side of Eq. (2.6) is from the BGK collision operator $(g-f)/\tau$. Then, Eq. (2.6) can be reformulated as

$$f\left(\boldsymbol{x}_{I+\frac{1}{2}},\boldsymbol{\xi},t+\delta t\right)=\frac{\delta t}{\tau+\delta t}g\left(\boldsymbol{x}_{I+\frac{1}{2}},\boldsymbol{\xi},t+\delta t\right)+\frac{\tau}{\tau+\delta t}f\left(\boldsymbol{x}_{I+\frac{1}{2}}-\boldsymbol{\xi}\delta t,\boldsymbol{\xi},t\right). \tag{2.7}$$

Eq. (2.7) reveals that the distribution function at the cell interface can be exactly calculated if $g(\boldsymbol{x}_{I+\frac{1}{2}},\boldsymbol{\xi},t+\delta t)$ (which is the equilibrium distribution function at the cell interface) and $f(\boldsymbol{x}_{I+\frac{1}{2}}-\boldsymbol{\xi}\delta t,\boldsymbol{\xi},t)$, (which is the initial distribution function at the surrounding points of cell interface) are both known. The accurate construction of f at the cell interface is the key issue for a successful calculation of numerical fluxes $\boldsymbol{F}$. This is also the main contribution of GKFS. In the following sections, we will focus on the way to construct the distribution function at the cell interface.

3 Initial distribution function approximated by the second-order polynomial in terms of 1, C, C^2

3.1 Motivations

As shown in Eq. (2.7), the construction of gas distribution function at the cell interface relies on $g(\boldsymbol{x}_{I+\frac{1}{2}},\boldsymbol{\xi},t+\delta t)$ and $f(\boldsymbol{x}_{I+\frac{1}{2}}-\boldsymbol{\xi}\delta t,\boldsymbol{\xi},t)$. The explicit formulation of equilibrium distribution function g is known, as shown in Eq. (2.2). Thus, the main issue is to construct the explicit formulation of initial gas distribution function $f(\boldsymbol{x}_{I+\frac{1}{2}}-\boldsymbol{\xi}\delta t,\boldsymbol{\xi},t)$. In the conventional GKFS, the initial distribution function of f is approximated by the first-order Chapman Enskog (CE) expansion analysis. Conventional GKFS is suitable for the simulation of flows at the thermodynamic equilibrium state, because the distribution function obtained by the first-order CE expansion could exactly recover the Navier-Stokes equations. However, when it comes to flows in the rarefied regime, the distribution function obtained from CE expansion is not sufficient to consider the strong non-equilibrium effect. To resolve the issue in the rarefied regime, a novel solver and a Grad's distribution function-based gas kinetic scheme have been proposed, in which the initial gas distribution function is approximated by the Grad's distribution function. Comparing with the conventional GKFS, these two solvers can be well applied for simulation of flows in the rarefied regime at a moderate Knudsen number.

Grad's distribution function is constructed based on the Hermite polynomial expansion. It is noteworthy that the accuracy of the novel solver and the Grad's distribution function-based gas kinetic scheme can be improved with higher order Hermite polynomial expansion used in the initial distribution function. However, the formulation of distribution function will be more complicated with higher order expansions. It is also noted that the Grad-26 based GKS does not improve the prediction of temperature as compared to the Grad-13 based GKS. This is because the additional higher-order terms in the Hermite polynomial expansion are not closely related to energy and thus have little contribution to the better prediction of temperature. To resolve this issue, a new way of constructing initial distribution function will be proposed in the next section.

3.2 Relationship between moments and peculiar velocity space of 1, C, C^2

From the perspective of gas kinetic theory, the most desirable macroscopic variables, such as density, momentum and energy can be calculated by taking the moments of g, $g(\boldsymbol{U}+\boldsymbol{C})$ and $\frac{1}{2}\cdot g(\boldsymbol{U}+\boldsymbol{C})^2$, respectively. Here, $\boldsymbol{U}$ is the mean velocity (reflecting the macroscopic physical information) and $\boldsymbol{C}$ is the peculiar velocity (reflecting the mesoscopic physical information). Thus, on the mesoscopic level, we can view $\mathbf{1}$, $\boldsymbol{C}$, $\boldsymbol{C}^{\mathbf{2}}$ as normalized particle mass, momentum and energy (normalized by g). It is also noted that all of the moments can be generally expressed as $\langle \boldsymbol{C}^m f\rangle$, where $\boldsymbol{C}^m$ represents a combination of peculiar velocity. Therefore, a natural way to construct the initial distribution function f is to take polynomial approximation in terms of $\mathbf{1}$, $\boldsymbol{C}$, $\boldsymbol{C}^{\mathbf{2}}$.

3.3 New way to construct initial distribution function

From both the CE expansion and the Hermite polynomial expansion, the gas distribution function f can be generally expressed as,

$$f = g\phi, \tag{3.1}$$

where, ϕ is a function. In the CE expansion, ϕ is related to the spatial derivatives of conservative variables and peculiar velocities. In the Hermite polynomial expansion, ϕ is connected with the high-order moments and peculiar velocities [30]. Considering that the expressions of ϕ involved in the two methods mentioned above are both associated with the peculiar velocities, we can approximate ϕ directly from the peculiar velocities. As discussed in the above section, $\mathbf{1}$, $\boldsymbol{C}$, $\boldsymbol{C^2}$ can be viewed as normalized particle mass, momentum and energy (normalized by g), which have inherent connection with the density, momentum, energy. Thus, in this work, the function ϕ is approximated by the second-order polynomial in terms of $\mathbf{1}$, $\boldsymbol{C}$, $\boldsymbol{C^2}$. For the two dimensional case, we just need to consider the peculiar velocities C_1 and C_2 in the x- and y- directions, and the peculiar velocity C_3 in the z-direction can be treated as the internal degree of freedom η. Therefore, the expression of $\boldsymbol{C}$ and $\boldsymbol{C^2}$ can be given as,

$$\boldsymbol{C} = \begin{bmatrix} C_1 & C_2 \end{bmatrix}, \tag{3.2a}$$

$$\boldsymbol{C}^2 = C_1^2 + C_2^2 + \eta^2. \tag{3.2b}$$

With the second-order polynomial approximation in terms of $\mathbf{1}$, $\boldsymbol{C}$, $\boldsymbol{C^2}$, the function ϕ can be generally written as,

$$\begin{aligned}\phi = &a_0\cdot 1 + a_1\cdot C_1 + a_2\cdot C_2 + a_3\cdot C_1C_1 + a_4\cdot C_2C_2 + a_5\cdot \boldsymbol{C}^2 \\ &+ a_6\cdot C_1C_2 + a_7\cdot C_1\boldsymbol{C}^2 + a_8\cdot C_2\boldsymbol{C}^2 + a_9\cdot \boldsymbol{C}^4.\end{aligned} \tag{3.3}$$

By substituting Eq. (3.2b) into Eq. (3.3), the function ϕ can be further reformulated as,

$$\begin{aligned}\phi = &a_0\cdot 1 + a_1\cdot C_1 + a_2\cdot C_2 + (a_3+a_5)\cdot C_1C_1 + (a_4+a_5)\cdot C_2C_2 + a_5\cdot \eta^2 \\ &+ a_6\cdot C_1C_2 + a_7\cdot C_1\boldsymbol{C}^2 + a_8\cdot C_2\boldsymbol{C}^2 + a_9\cdot \boldsymbol{C}^4.\end{aligned} \tag{3.4}$$

To make the formulation shown in Eq. (3.4) be more compact, the following relations can be defined as

$$a_0 = \tilde{a}_0, \quad a_1 = \tilde{a}_1, \quad a_2 = \tilde{a}_2, \quad a_3 + a_5 = \tilde{a}_3, \quad a_4 + a_5 = \tilde{a}_4, \tag{3.5a}$$

$$a_5 = \tilde{a}_5, \quad a_6 = \tilde{a}_6, \quad a_7 = \tilde{a}_7, \quad a_8 = \tilde{a}_8, \quad a_9 = \tilde{a}_9. \tag{3.5b}$$

Substituting the relations in Eq. (3.5) into Eq. (3.4), the function ϕ can be rewritten as,

$$\begin{aligned}\phi = &\tilde{a}_0\cdot 1 + \tilde{a}_1\cdot C_1 + \tilde{a}_2\cdot C_2 + \tilde{a}_3\cdot C_1^2 + \tilde{a}_4\cdot C_2^2 + \tilde{a}_5\cdot \eta^2 \\ &+ \tilde{a}_6\cdot C_1C_2 + \tilde{a}_7\cdot C_1\boldsymbol{C}^2 + \tilde{a}_8\cdot C_2\boldsymbol{C}^2 + \tilde{a}_9\cdot \boldsymbol{C}^4.\end{aligned} \tag{3.6}$$

By Combining Eq. (3.6) with Eq. (3.1), the initial distribution function approximated by the second-order polynomial in terms of $\mathbf{1}$, $\boldsymbol{C}$, $\boldsymbol{C^2}$ can be written as,

$$f=g\cdot\begin{pmatrix}\tilde{a}_0\cdot 1+\tilde{a}_1\cdot C_1+\tilde{a}_2\cdot C_2+\tilde{a}_3\cdot C_1^2+\tilde{a}_4\cdot C_2^2+\tilde{a}_5\cdot\eta^2\\ +\tilde{a}_6\cdot C_1C_2+\tilde{a}_7\cdot C_1\boldsymbol{C}^2+\tilde{a}_8\cdot C_2\boldsymbol{C}^2+\tilde{a}_9\cdot\boldsymbol{C}^4\end{pmatrix}. \tag{3.7}$$

The unknown coefficients $\tilde{a}_i$ $(i=0,\ldots,9)$ in Eq. (3.7) can be determined by the compatibility conditions and moment relationships which are robust in all flow regimes. From the compatibility condition, we have

$$\begin{bmatrix}\langle f\rangle\\ \langle f\boldsymbol{\xi}\rangle\\ \left\langle f|\boldsymbol{\xi}|^2/2\right\rangle\end{bmatrix}=\begin{bmatrix}\langle g\rangle\\ \langle g\boldsymbol{\xi}\rangle\\ \left\langle g|\boldsymbol{\xi}|^2/2\right\rangle\end{bmatrix}=\begin{bmatrix}\rho\\ \rho\boldsymbol{U}\\ \rho E\end{bmatrix}. \tag{3.8}$$

By substituting Eq. (3.7) into $\langle f\rangle=\langle g\rangle=\rho$, we can obtain

$$\tilde{a}_0+(\tilde{a}_3+\tilde{a}_4+\tilde{a}_5)RT+15(RT)^2\cdot\tilde{a}_9=1. \tag{3.9}$$

Next, by substituting Eq. (3.7) into $\langle f\boldsymbol{\xi}\rangle=\langle g\boldsymbol{\xi}\rangle=\rho\boldsymbol{U}$, we have

$$\tilde{a}_1=-5RT\cdot\tilde{a}_7, \tag{3.10a}$$
$$\tilde{a}_2=-5RT\cdot\tilde{a}_8. \tag{3.10b}$$

Finally, by substituting Eq. (3.7) into

$$\langle f|\boldsymbol{\xi}|^2/2\rangle=\langle g|\boldsymbol{\xi}|^2/2\rangle=\rho E,$$

we can obtain

$$\tilde{a}_3+\tilde{a}_4+\tilde{a}_5+30(RT)\cdot\tilde{a}_9=0. \tag{3.11}$$

The moment relationship derive the following relations

$$\langle f\rangle=\langle g\cdot\phi\rangle, \tag{3.12a}$$
$$\langle f\cdot C_1\rangle=\langle g\cdot\phi\cdot C_1\rangle,\qquad \langle f\cdot C_2\rangle=\langle g\cdot\phi\cdot C_2\rangle, \tag{3.12b}$$
$$\langle f\cdot C_1^2\rangle=\langle g\cdot\phi\cdot C_1^2\rangle,\qquad \langle f\cdot C_2^2\rangle=\langle g\cdot\phi\cdot C_2^2\rangle, \tag{3.12c}$$
$$\langle f\cdot\eta^2\rangle=\langle g\cdot\phi\cdot\eta^2\rangle,\qquad \langle f\cdot C_1C_2\rangle=\langle g\cdot\phi\cdot C_1C_2\rangle, \tag{3.12d}$$
$$\langle f\cdot C_1\boldsymbol{C}^2\rangle=\langle g\cdot\phi\cdot C_1\boldsymbol{C}^2\rangle,\qquad \langle f\cdot C_2\boldsymbol{C}^2\rangle=\langle g\cdot\phi\cdot C_2\boldsymbol{C}^2\rangle, \tag{3.12e}$$
$$\left\langle f\cdot\boldsymbol{C}^4\right\rangle=\left\langle g\cdot\phi\cdot\boldsymbol{C}^4\right\rangle. \tag{3.12f}$$

By substituting the expression of ϕ shown in Eq. (3.6) into Eqs. (3.12a)-(3.12f), and with the help of relations shown in Eqs. (3.9)-(3.11), all of the coefficients shown in Eq. (3.6) can be exactly calculated and listed as follows,

$$\tilde{a}_0=1+15(RT)^2\tilde{a}_9,\quad \tilde{a}_1=-\frac{\langle fC_1\boldsymbol{C}^2\rangle}{2\rho(RT)^2},\quad \tilde{a}_2=-\frac{\langle fC_2\boldsymbol{C}^2\rangle}{2\rho(RT)^2}, \tag{3.13a}$$

$$\tilde{a}_3=\frac{\langle fC_1^2\rangle}{2\rho(RT)^2}-\frac{1}{2RT}-10\tilde{a}_9RT,\quad \tilde{a}_4=\frac{\langle fC_2^2\rangle}{2\rho(RT)^2}-\frac{1}{2RT}-10\tilde{a}_9RT, \tag{3.13b}$$

$$\tilde{a}_5=\frac{\langle fC_3^2\rangle}{2\rho(RT)^2}-\frac{1}{2RT}-10\tilde{a}_9RT,\quad \tilde{a}_6=\frac{\langle fC_1C_2\rangle}{\rho(RT)^2},\quad \tilde{a}_7=\frac{\langle fC_1\boldsymbol{C}^2\rangle}{10\rho(RT)^3}, \tag{3.13c}$$

$$\tilde{a}_8=\frac{\langle fC_2\boldsymbol{C}^2\rangle}{10\rho(RT)^3},\quad \tilde{a}_9=\frac{\langle \boldsymbol{C}^4 f\rangle}{120\rho(RT)^4}-\frac{1}{8(RT)^2}. \tag{3.13d}$$

4 Gas kinetic flux solver based on new initial distribution function

In Section 3.2, a new initial distribution function has been constructed. A natural question is that weather we can replace the Grad's distribution function with the newly derived one and then construct a new gas kinetic flux solver. In this section, we will answer this question.

4.1 Determination of equilibrium distribution function at the cell interface

As seen in Eq. (2.2), the equilibrium distribution function is the function of density, velocity and temperature. Hence, to calculate the equilibrium distribution function at the cell interface, we just need to determine the vector of macroscopic flow variables $\boldsymbol{W}_{I+\frac{1}{2}}$ at the cell interface. Based on the compatibility condition, $g(\boldsymbol{x}_{I+\frac{1}{2}},\boldsymbol{\xi},t+\delta t)$ and $f(\boldsymbol{x}_{I+\frac{1}{2}},\boldsymbol{\xi},t+\delta t)$ satisfy the conservation constraint, which yields

$$\left\langle \boldsymbol{\varphi}\left(g\left(\boldsymbol{x}_{I+\frac{1}{2}},\boldsymbol{\xi},t+\delta t\right)-f\left(\boldsymbol{x}_{I+\frac{1}{2}},\boldsymbol{\xi},t+\delta t\right)\right)\right\rangle=0. \tag{4.1}$$

Substituting the expression of $f(\boldsymbol{x}_{I+\frac{1}{2}},\boldsymbol{\xi},t+\delta t)$ given in Eq. (2.7) into Eq. (4.1), the equation above can be reformulated as

$$\left\langle \boldsymbol{\varphi}g\left(\boldsymbol{x}_{I+\frac{1}{2}},\boldsymbol{\xi},t+\delta t\right)\right\rangle=\left\langle \boldsymbol{\varphi}f\left(\boldsymbol{x}_{I+\frac{1}{2}}-\boldsymbol{\xi}\delta t,\boldsymbol{\xi},t\right)\right\rangle, \tag{4.2}$$

which means that the macroscopic variables $\boldsymbol{W}_{I+\frac{1}{2}}$ at the cell interface can be calculated by moments of initial distribution function at surrounding points. Hence, the key issue to construct the distribution function at the cell interface also relies on the distribution function $f(\boldsymbol{x}_{I+\frac{1}{2}}-\boldsymbol{\xi}\delta t,\boldsymbol{\xi},t)$. The methodology to construct the initial distribution function

at the surrounding points should be the main contribution of present paper and will be discussed in detail in the following section.

4.2 Construction of initial distribution function at surrounding points of cell interface

As shown in Eq. (3.7), the new derived distribution function depends on the coefficients $\tilde{a}_i$ $(i=0,\ldots,9)$. Hence, to construct the initial gas distribution function at the surrounding points, we just need to focus on the coefficients at $\boldsymbol{x}_{I+\frac{1}{2}}-\boldsymbol{\xi}\delta t$. Here, we adopt $\boldsymbol{A}(\boldsymbol{x}_{I+\frac{1}{2}}-\boldsymbol{\xi}\delta t,t)$ to represent the vector of these coefficients located at $\boldsymbol{x}_{I+\frac{1}{2}}-\boldsymbol{\xi}\delta t$. The coefficients can be calculated by,

$$\boldsymbol{A}\left(\boldsymbol{x}_{I+\frac{1}{2}}-\boldsymbol{\xi}\delta t,t\right)=\begin{cases}\boldsymbol{A}_L\left(\boldsymbol{x}_{I+\frac{1}{2}},t\right)-\nabla\boldsymbol{A}_L\left(\boldsymbol{x}_{I+\frac{1}{2}},t\right)\cdot\boldsymbol{\xi}\delta t, & \xi_n>0,\\ \boldsymbol{A}_R\left(\boldsymbol{x}_{I+\frac{1}{2}},t\right)-\nabla\boldsymbol{A}_R\left(\boldsymbol{x}_{I+\frac{1}{2}},t\right)\cdot\boldsymbol{\xi}\delta t, & \xi_n<0,\end{cases} \tag{4.3}$$

where the subscripts L and R are the values of vector A at the left and the right sides of the interface, respectively. $\nabla\boldsymbol{A}$ stands for the gradient of $\boldsymbol{A}$. To ensure second-order accuracy, the values of $\nabla\boldsymbol{A}_L(\boldsymbol{x}_{I+\frac{1}{2}},t)$ and $\nabla\boldsymbol{A}_R(\boldsymbol{x}_{I+\frac{1}{2}},t)$ can be approximated by $\nabla\boldsymbol{A}(\boldsymbol{x}_I,t)$ and $\nabla\boldsymbol{A}(\boldsymbol{x}_{I+1},t)$, respectively. Here, $\boldsymbol{x}_I$ represents the location of center of cell I, which is at the left side of cell interface $\boldsymbol{x}_{I+\frac{1}{2}}$. $\boldsymbol{x}_{I+1}$ means the location of center of cell $I+1$, which is on the right side of cell interface $\boldsymbol{x}_{I+\frac{1}{2}}$.Their first-order derivatives can be easily calculated by the central difference scheme.

After that, the values of vector $\boldsymbol{A}$ on the left and the right sides of the interface could be obtained by interpolation from the values at cell centers as,

$$\boldsymbol{A}_L\left(\boldsymbol{x}_{I+\frac{1}{2}},t\right)=\boldsymbol{A}(\boldsymbol{x}_I,t)+\frac{\partial A(\boldsymbol{x}_I,t)}{\partial x}\cdot\left(\boldsymbol{x}_{I+\frac{1}{2}}-\boldsymbol{x}_I\right), \tag{4.4a}$$

$$\boldsymbol{A}_R\left(\boldsymbol{x}_{I+\frac{1}{2}},t\right)=\boldsymbol{A}(\boldsymbol{x}_{I+1},t)+\frac{\partial A(\boldsymbol{x}_{I+1},t)}{\partial x}\cdot\left(\boldsymbol{x}_{I+\frac{1}{2}}-\boldsymbol{x}_{I+1}\right). \tag{4.4b}$$

Once the values of vector $\boldsymbol{A}$ at the surrounding points of cell interface are all known, the gas distribution function around the cell interface can be determined subsequently.

With the reconstruction of $f(\boldsymbol{x}_{I+\frac{1}{2}}-\boldsymbol{\xi}\delta t,\boldsymbol{\xi},t)$, the conservative variables at the cell interface can be calculated by Eq. (4.2). Then, the equilibrium distribution function $g(\boldsymbol{x}_{I+\frac{1}{2}},\boldsymbol{\xi},t+\delta t)$ at the cell interface could be determined by Eq. (2.2). With $f(\boldsymbol{x}_{I+\frac{1}{2}}-\boldsymbol{\xi}\delta t,\boldsymbol{\xi},t)$ and $g(\boldsymbol{x}_{I+\frac{1}{2}},\boldsymbol{\xi},t+\delta t)$ both known, the distribution function at the cell interface can be calculated according to Eq. (2.7).

4.3 The method to update the coefficients at cell centers

At the first time step, we suppose that the system is at the equilibrium state. Hence, all coefficients in Eqs. (3.13a)-(3.13d) can be initialized at the equilibrium state with $\tilde{a}_0=1$

and $\tilde{a}_i = 0$ ($i = 1,\ldots,9$). Then, in the following time steps, all of the coefficients at the cell centre should be updated. The methodology to update the coefficients will be clarified into two steps, as follows

Step 1. Calculate the coefficients at the cell interface through moment relationship directly. According to the expressions of the coefficients shown in Eqs. (3.13a)-(3.13d), it is noted that all of the coefficients are related to the moments of gas distribution function, macroscopic density and macroscopic temperature. As shown in Eq. (2.7), the gas distribution function at the cell interface could be accurately constructed. Then, the coefficients at the cell interface could be calculated by the moment relationship directly. Taking the coefficient $\tilde{a}_9$ as an example, its value at the cell interface can be calculated by $\tilde{a}_{9,I+\frac{1}{2}} = \langle \boldsymbol{C}^4 \cdot f(\boldsymbol{x}_{I+\frac{1}{2}}, \boldsymbol{\xi}, t+\delta t) \rangle$. By using the expression of gas distributions f^L, f^R, f^U and f^B at four cell interfaces that enclose the control cell, its value at the left, right, upper and bottom interfaces could be calculated as follows

$$\tilde{a}_9^L = \left\langle \boldsymbol{C}^4 f^L \right\rangle, \tag{4.5a}$$

$$\tilde{a}_9^R = \left\langle \boldsymbol{C}^4 f^R \right\rangle, \tag{4.5b}$$

$$\tilde{a}_9^U = \left\langle \boldsymbol{C}^4 f^U \right\rangle, \tag{4.5c}$$

$$\tilde{a}_9^B = \left\langle \boldsymbol{C}^4 f^B \right\rangle. \tag{4.5d}$$

Other moments at the cell interface, including $\langle C_1^2 f \rangle$, $\langle C_2^2 f \rangle$, $\langle \eta^2 f \rangle$, $\langle C_1 C_2 f \rangle$, $\langle C_1 \boldsymbol{C}^2 f \rangle$ and $\langle C_2 \boldsymbol{C}^2 f \rangle$ could be calculated in the same way.

Similarly, the conservative variables $\boldsymbol{W} = (\rho, \rho U, \rho V, \rho E)$ at the cell interface can be calculated by $\langle \boldsymbol{\varphi} f^L \rangle$, $\langle \boldsymbol{\varphi} f^R \rangle$, $\langle \boldsymbol{\varphi} f^U \rangle$ and $\langle \boldsymbol{\varphi} f^B \rangle$. Then, the density and temperature at the cell interface can be calculated by,

$$\rho = W_1, \tag{4.6a}$$

$$T = \frac{\left[2W_4 W_1 - \left(W_2^2 + W_3^2\right)\right](\gamma - 1)}{2W_1^2 R}, \tag{4.6b}$$

where γ is the specific heat ratio and equals to $5/3$ for monatomic gas.

Step 2. Update the coefficients at the cell center. On the uniform mesh, the moment $\tilde{a}_9^C$ at the cell center could be evaluated by averaging the values at surrounding four cell interfaces as

$$\tilde{a}_9^C = \frac{1}{4}\left(\tilde{a}_9^L + \tilde{a}_9^R + \tilde{a}_9^U + \tilde{a}_9^B\right). \tag{4.7}$$

The other moments at the cell center can be updated in the same way. By substituting the updated values into Eqs. (3.13a)-(3.13d), the values of the coefficients at the cell interface can be updated and the distribution function at the cell centre can be updated, subsequently.

4.3.1 Numerical approximation of integrals

In the present GKFS, the computation of macroscopic variables, flux vector and the coefficients relies on the moment integrals of distribution function in the particle velocity space. Theoretically, analytical forms of integrals for the new derived gas distribution function can be given out. For simplicity, numerical quadrature is applied for approximation of integrals in this work. Analytical forms of integrals for the solver can be explored in the future to reduce computational efforts.

For low speed flows with small temperature variation, the high-order Gauss-Hermite quadrature rule [31,32] is a proper choice to approximate integrals. To compute the conservative variables, numerical fluxes and the coefficients, we need to discretize the particle velocity space into a set of discrete velocities $\boldsymbol{\xi}_\alpha$. By applying the integral quadrature, the vector of conservative variables $\boldsymbol{W}$ at the cell interface can be approximately calculated by,

$$\boldsymbol{W} \approx \sum_\alpha w_\alpha \boldsymbol{\varphi}_\alpha f\left(\boldsymbol{x}_{I+\frac{1}{2}} - \boldsymbol{\xi}_\alpha \delta t, \boldsymbol{\xi}_\alpha, t\right). \tag{4.8}$$

Here, w_α is the quadrature weight and $\boldsymbol{\varphi}_\alpha$ is equal to $(1, \boldsymbol{\xi}_\alpha, \boldsymbol{\xi}_\alpha^2/2)$. Similarly, numerical fluxes at the cell interface can be approximately computed by

$$\boldsymbol{F} \approx \sum_\alpha w_\alpha \boldsymbol{\xi}_\alpha \boldsymbol{\varphi}_\alpha \left(\frac{\delta t}{\tau + \delta t} g\left(\boldsymbol{x}_{I+\frac{1}{2}}, \boldsymbol{\xi}_\alpha, t+\delta t\right) + \frac{\tau}{\tau+\delta t} f\left(\boldsymbol{x}_{I+\frac{1}{2}} - \boldsymbol{\xi}_\alpha \delta t, \boldsymbol{\xi}_\alpha, t\right)\right). \tag{4.9}$$

The coefficients shown in Eqs. (3.13a)-(3.13d) can also be rewritten in the form of numerical quadrature. Taking the coefficient $\tilde{a}_9$ as an example, we have

$$\tilde{a}_9 \approx \sum_\alpha w_\alpha \boldsymbol{C}_\alpha^4 \left(\frac{\delta t}{\tau + \delta t} g\left(\boldsymbol{x}_{I+\frac{1}{2}}, \boldsymbol{\xi}_\alpha, t+\delta t\right) + \frac{\tau}{\tau+\delta t} f\left(\boldsymbol{x}_{I+\frac{1}{2}} - \boldsymbol{\xi}_\alpha \delta t, \boldsymbol{\xi}_\alpha, t\right)\right), \tag{4.10}$$

where $\boldsymbol{C}_\alpha$ is equivalent to $\boldsymbol{U} - \boldsymbol{\xi}_\alpha$.

Here, we also need to elaborate the methodology to calculate τ and δt. As indicated in Eq. (2.1), τ is the ratio of dynamic viscosity μ to pressure p. To determine μ and p at the cell interface, the density ρ and temperature T at the cell interface should be calculated. As seen in Eq. (4.8), the vector of conservative variables W at the cell interface has been approximated by numerical approximation, thus ρ and T can be obtained by Eq. (4.6a) and Eq. (4.6b), subsequently.

The main constraint for δt is to restrict the local streaming points within the neighboring cells. To satisfy this condition, δt can be computed by

$$\delta t \leq \frac{\min\{\Delta \boldsymbol{x}\}}{2\max\{|\boldsymbol{\xi}_\alpha|\}}, \tag{4.11}$$

where $\Delta \boldsymbol{x} = (\Delta x, \Delta y)$ is grid spacing in x- and y-direction. $\max\{|\boldsymbol{\xi}_\alpha|\}$ represents the maximum value of discrete velocities.

4.4 Implementation of kinetic boundary conditions

To evaluate numerical fluxes at the boundary, the distribution function at the boundary point should be determined. In this work, the Maxwell's kinetic boundary condition with perfect thermalizing wall [33] is considered, in which, the gas molecules will be diffusively reflected with a Maxwellian distribution at the wall temperature. Thus, the distribution function reflected from the wall can be given as

$$f(\boldsymbol{x}_W,\boldsymbol{\xi}_\alpha,t)=\frac{\rho_W}{(2\pi RT_W)^{\frac{3}{2}}}\cdot\exp\left[-\frac{(\boldsymbol{\xi}_\alpha-\boldsymbol{U}_W)^2}{2RT_W}\right], \tag{4.12}$$

where $\boldsymbol{x}_W$, T_W and $\boldsymbol{U}_W$ are the position, temperature and velocity of the wall, respectively. ρ_W is the density on the wall, which can be determined from the no-penetration condition as follows

$$\sum_{\alpha}^{\boldsymbol{\xi}_\alpha\cdot\boldsymbol{n}_W\geq 0} w_\alpha\cdot\boldsymbol{\xi}_\alpha\cdot\boldsymbol{n}_W\cdot f(\boldsymbol{x}_W,\boldsymbol{\xi}_\alpha,t)+\sum_{\alpha}^{\boldsymbol{\xi}_\alpha\cdot\boldsymbol{n}_W<0} w_\alpha\cdot\boldsymbol{\xi}_\alpha\cdot\boldsymbol{n}_W\cdot f(\boldsymbol{x}_W-\boldsymbol{\xi}_\alpha\delta t,\boldsymbol{\xi}_\alpha,t)=0, \tag{4.13}$$

where $\boldsymbol{n}_W$ stands for the normal vector of the wall pointing towards the flow field. $f(\boldsymbol{x}_W-\boldsymbol{\xi}_\alpha\delta t,\boldsymbol{\xi}_\alpha,t)$ means the incident distribution function in the flow domain, which is reconstructed by the new derived gas distribution function. By substituting the expression of $f(\boldsymbol{x}_W,\boldsymbol{\xi}_\alpha,t)$ and $f(\boldsymbol{x}_W-\boldsymbol{\xi}_\alpha\delta t,\boldsymbol{\xi}_\alpha,t)$ into Eq. (4.13), the density at the wall surface can be calculated as [34]

$$\rho_W=-\frac{\sum_{\alpha}^{\boldsymbol{\xi}_\alpha\cdot\boldsymbol{n}_W<0} w_\alpha\cdot\boldsymbol{\xi}_\alpha\cdot\boldsymbol{n}_W\cdot f(\boldsymbol{x}_W-\boldsymbol{\xi}_\alpha\delta t,\boldsymbol{\xi}_\alpha,t)}{\frac{1}{(2\pi RT_W)^{\frac{3}{2}}}\sum_{\alpha}^{\boldsymbol{\xi}_\alpha\cdot\boldsymbol{n}_W\geq 0} w_\alpha\cdot\boldsymbol{\xi}_\alpha\cdot\boldsymbol{n}_W\cdot\exp\left[-\frac{(\boldsymbol{\xi}_\alpha-\boldsymbol{U}_W)^2}{2RT_W}\right]}. \tag{4.14}$$

With the gas distribution function at the boundary, the numerical fluxes can be calculated accordingly.

4.5 Computational procedure

The computational sequence of the present GKFS can be summarized as follows:

(1) Calculate the first order derivatives of coefficients at each cell center and determine their values at the surrounding points of cell interface by the interpolation as shown in Eq. (4.3).

(2) Reconstruct the initial gas distribution function at the surrounding points of each cell interface by the new derived gas distribution function using Eq. (3.7).

(3) Compute the conservative variables $\boldsymbol{W}_{I+\frac{1}{2}}$ at cell interface using Eq. (4.2). Then, calculate the distribution function $g(\boldsymbol{x}_{I+\frac{1}{2}},\boldsymbol{\xi},t+\delta t)$ at equilibrium state by Eq. (2.2).

(4) Reconstruct the distribution function $f(\boldsymbol{x}_{I+\frac{1}{2}},\boldsymbol{\xi},t+\delta t)$ at cell interface using Eq. (2.7) and update the coefficients by the method shown in Section 4.3.

(5) Calculate the density at the wall using Eq. (4.14) and then implement the kinetic boundary conditions as discussed in Section 4.5.

(6) Solve the ordinary differential equation shown in Eq. (2.5) by the third-order TVD Runge-Kutta method.

(7) Repeat steps (1)-(6) until the computation converges with the residual less than 10^{-6}.

5 Numerical examples

In this section, the present solver is utilized to simulate some classical cases to validate its accuracy from the continuum regime to the transition regime. The benchmark data for the numerical validation is given by the results of DVM [35] due to its high accuracy in the whole flow regimes. We need to clarify that the DVM results in present paper are all obtained by using 28×28 quadrature points in the particle velocity space.

Case 1: Planar Couette flow.

The simulation of planar Couette flow is conducted as the first case to test the performance of present solver. In the rarefied regime, this classical case contains Knudsen layer effect, which results in the nonlinear velocity profile near the moving boundary. This case has also been tested by Gu and Emerson [22] for the validation of regularized moment equations and Liu et al. [23] for the validation of a novel solver. As shown in Fig. 1, the upper and lower walls are set at the location of $y=\pm H/2$ and moving with the velocity of $U_w=\pm50\text{m/s}$. The temperatures for the two moving walls are both fixed at $T_w=273\text{K}$. The left and right boundaries are periodic. The computational domain is divided uniformly into 60×60 cells and the numerical integration is approximated by Gauss-Hermite quadrature with 8×8 mesh points.

Three cases with different Knudsen numbers of 0.1, 0.25 and 0.5 are considered. Herein, the Knudsen number is defined as the ratio of molecular mean free path (λ) to the characteristic length (H) [36],

$$Kn=\lambda/H, \tag{5.1}$$

in which, λ can be further expressed by the reference viscosity (μ_0) and reference temperature ($T_0=273\text{K}$) as,

$$\lambda=\frac{\mu_0}{p}\sqrt{\frac{\pi RT_0}{2}}. \tag{5.2}$$

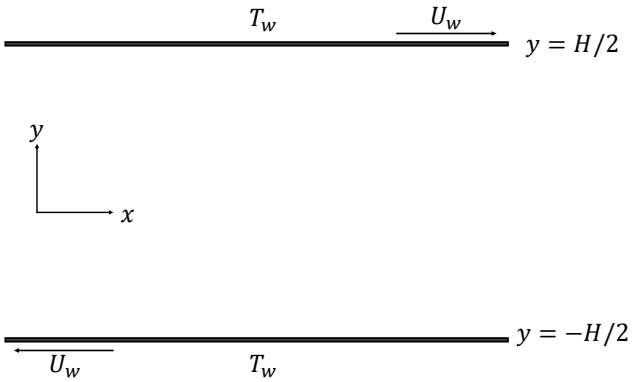

Figure 1: Schematic of planar Couette flow.

By substituting Eq. (5.1) into Eq. (5.2), the reference viscosity μ_0 can be determined by,

$$\mu_0 = Kn \cdot H \cdot p \sqrt{\frac{2}{\pi R T_0}}. \tag{5.3}$$

Then, the viscosity in the flow pattern can be calculated by Sutherland's law [37] as

$$\mu = \mu_0 \left(\frac{T}{T_0}\right)^{15} \frac{T_0 + T_s}{T + T_s}, \tag{5.4}$$

where $T_s = 104K$ for argon gas.

As shown in Fig. 2, the velocity profile obtained by present solver is compared with those from regularized 13 moment (R-13) equations and novel solver. It is found that the velocity near the upper and lower moving walls is about $\pm 41\text{m/s}$, which differs from the velocity of moving wall. This indicates that the wall slip phenomenon indeed occurs at Kn$=0.1$, which belongs to the slip regime. In the zoom-in view of Fig. 2, the shape of velocity profiles inside the Knudsen layer can be seen more clearly. Both the NS equations and the R-13 equations fail to capture the nonlinear effect, whereas the present solver as well as the novel solver can predict the nonlinear velocity profile. Fig. 3 shows the comparison of velocity profiles in early transition regime at Kn$= 0.25$. In this state, the velocity near the boundary is about $\pm 34\text{m/s}$. This means that by increasing the Knudsen number, the slip at wall will be enlarged. From the zoom-in view in Fig. 3, we can find that the present solver and the novel solver can predict the power-law behavior of velocity profile. As seen in Fig. 4, when the Knudsen number reaches the transition regime at Kn$= 0.5$, the Knudsen layer effect will become extremely strong. The velocity profiles predicted by the present solver and the novel solver still follow the nonlinear effect within the Knudsen layer. The deficiencies of NS and R-13 equations are more obvious in this scenario, which can be seen in the zoom-in view in Fig. 4. This case validates that the

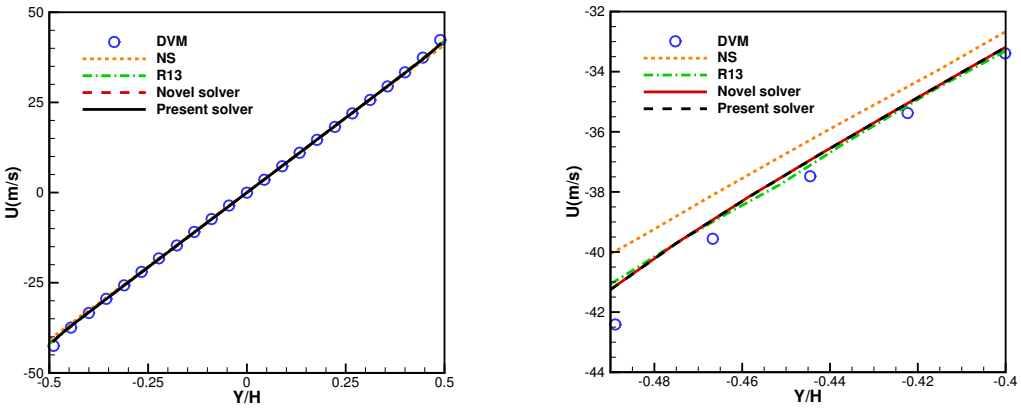

Figure 2: Comparison of velocity profiles (left) and zoom-in view (right) for Kn$=0.1$.

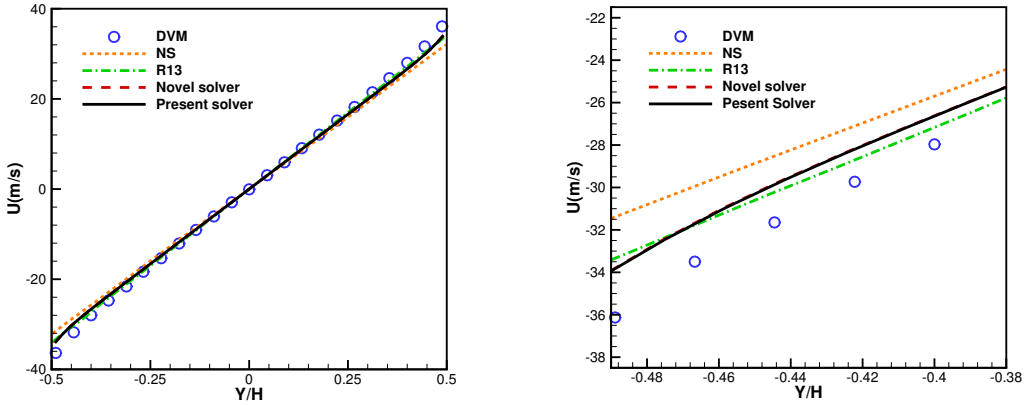

Figure 3: Comparison of velocity profiles (left) and zoom-in ones (right) for Kn$=0.25$.

present distribution function can capture the rarefication effect for the non-equilibrium flows till the transition flow regime, and the accuracy of obtained velocity profiles is comparable to the novel solver.

Case 2: Lid-driven cavity flow.

The second case is a two-dimensional lid-driven cavity flow. The schematic diagram is shown in Fig. 5, which is a square enclosure with length L. The top wall is moving with the velocity of $U_w = 50\text{m/s}$ and the other walls are stationary. All walls are considered isothermal with a fixed temperature of T_w=273K. This case can reflect most features of the rarefaction effect, and thus has been simulated by Rana et al. [38] using R-13 equations

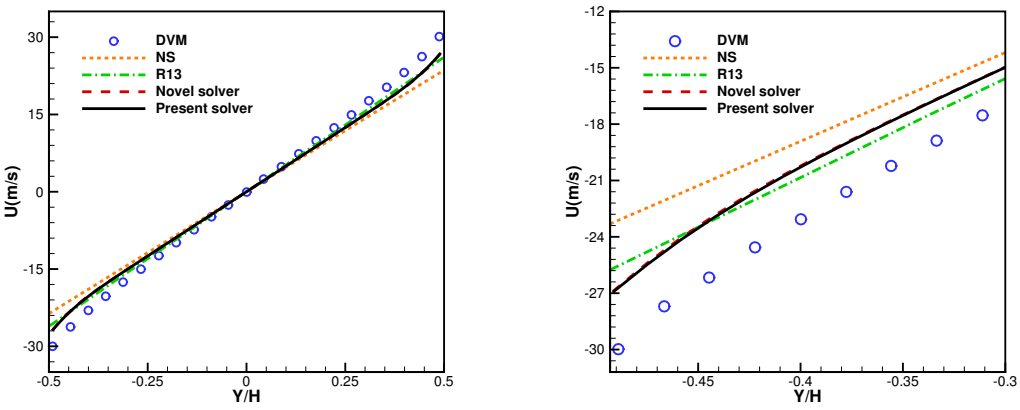

Figure 4: Comparison of velocity profiles (left) and zoom-in ones (right) for Kn$=0.5$.

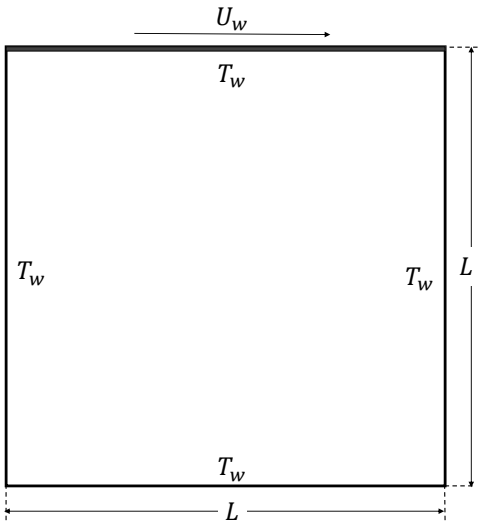

Figure 5: Schematic of lid-driven cavity flow.

and Liu et al. [23] using the novel solver. For this case, the computational region is also divided uniformly into 60×60 cells and the particle velocity space is discretized by 8×8 quadrature points.

In this case, the characteristic length is chosen as L. Thus, the Knudsen number is computed by

$$Kn=\lambda/L, \tag{5.5}$$

in which, the molecular mean free path (λ) is the function of reference viscosity (μ_0),

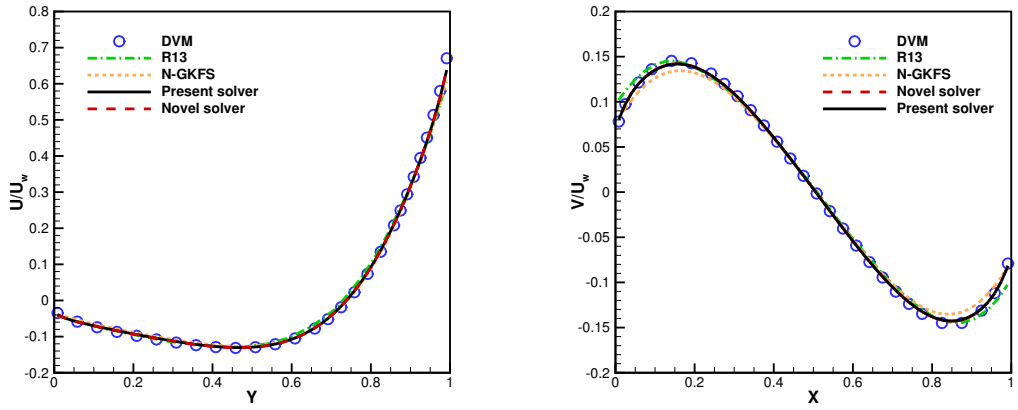

Figure 6: Comparison of U-velocity profiles along vertical centerline (left) and V-velocity profiles along horizontal centerline (right) for Kn$=0.0798$.

reference temperature (T_0) and reference density (ρ_0). It can be calculated by

$$\lambda = \frac{\mu_0}{\rho_0\sqrt{RT_0}}. \tag{5.6}$$

By substituting Eq. (5.6) into Eq. (5.5), the reference viscosity can be reformulated as,

$$\mu_0 = Kn \cdot L \cdot \rho_0\sqrt{RT_0}. \tag{5.7}$$

To make a comparison with the results shown in [23] and [38], the Knudsen numbers of Kn$=0.0798$ and 0.3989 are selected. After the reference viscosity is determined, the viscosity (μ) in the flow field can be calculated [39] by,

$$\mu = \mu_0\left(\frac{T}{T_0}\right)^{\omega}, \tag{5.8}$$

where the viscosity exponent ω is equal to 1.

Fig. 6 illustrates the comparison of the velocity profiles along the centerline for Kn$=0.0798$. As seen in the left plot, the U-velocity profiles obtained by different methods match well with each other. However, there exists some difference for the V-velocity profile as shown in the right plot of Fig. 6. Comparing with the result of DVM, R-13 equations slightly over-predict the V-velocity near the boundary, while, the result which is predicted by novel gas kinetic flux solver [18], under-predicts the peak value of V-velocity. In contrast, V-velocity predicted by present solver can be in good agreement with the results of the novel solver and DVM. Figs. 7(a), (b) and (c) show the comparison of temperature contour and heat flux streamlines obtained by the present solver, the novel solver and the DVM, respectively. We can see that all of the three methods can well

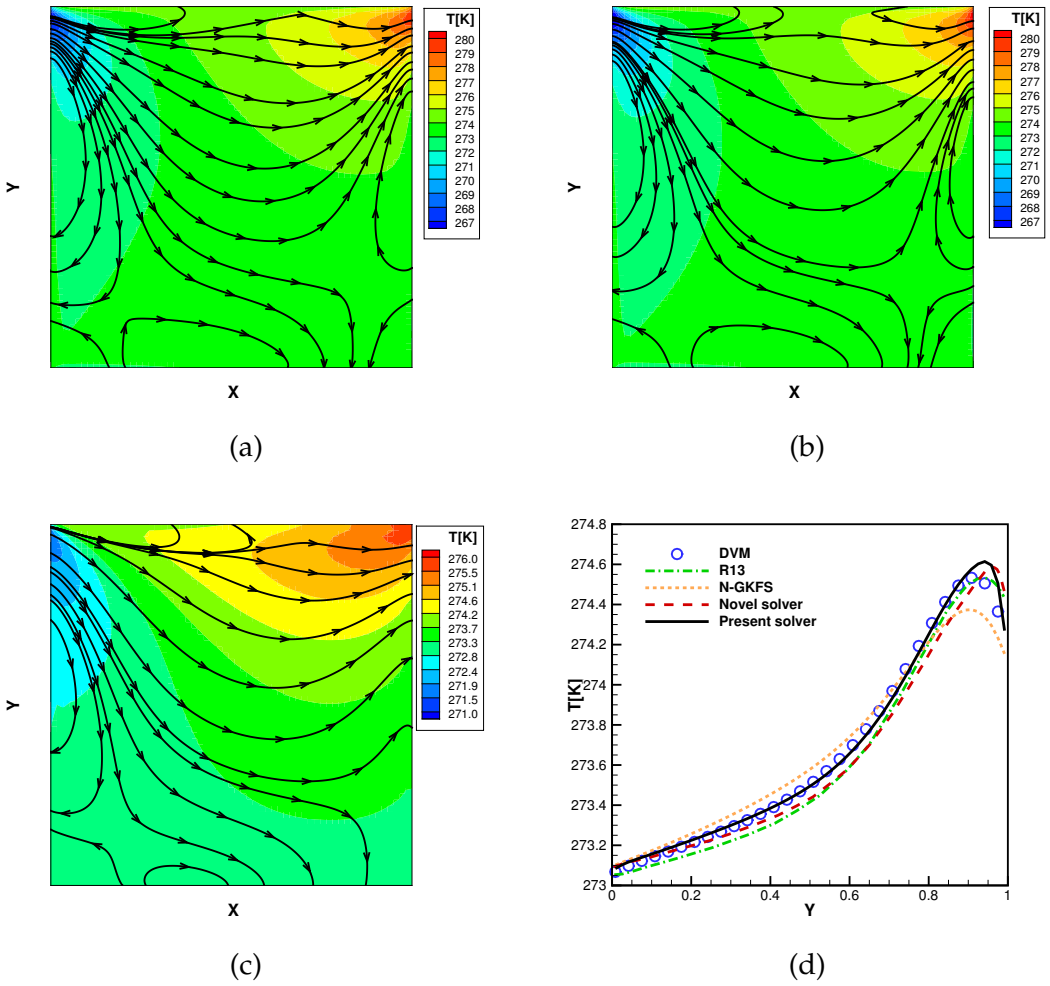

Figure 7: Temperature contours overlaid with heat flux streamlines and profiles for Kn = 0.0798: (a) present solver, (b) novel solver, (c) DVM, (d) temperature profiles along vertical central line.

predict the anti-Fourier heat transfer phenomenon, which means that the streamlines of heat flux go from the left upper corner (low temperature region) to the right upper corner (high temperature region). In Fig. 7(d), the comparison of temperature profiles along the vertical centerline is shown in detail. The thermal behavior predicted by the present solver agrees well with that from DVM. Both R-13 equations and the novel solver underestimate the temperature in the bottom region and over-predict the temperature near the wall boundary. From this aspect, the gas distribution function approximated by the second-order polynomial in terms of $\mathbf{1}$, $\boldsymbol{C}$, $\boldsymbol{C}^2$ performs better than the Grad's 13-moment distribution for the prediction of temperature profiles. Additionally, the effect of quadra-

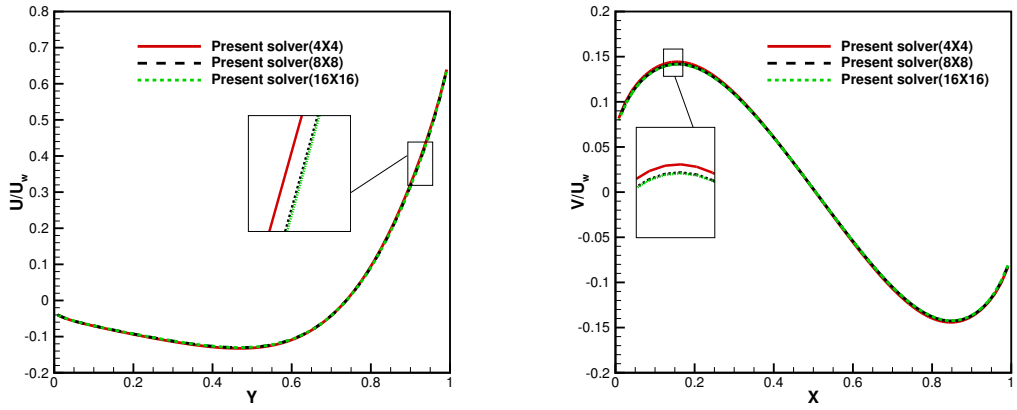

Figure 8: Comparison of U-velocity (left) and V-velocity (right) profiles with different quadrature points at Kn$=0.0798$.

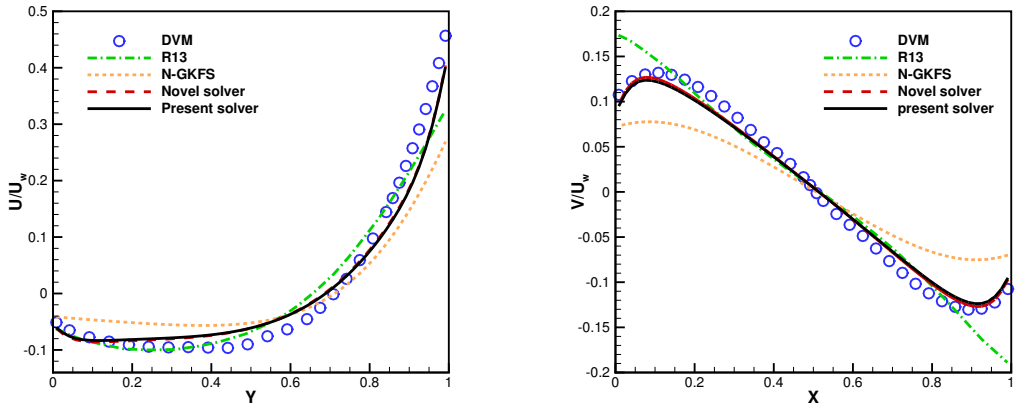

Figure 9: Comparison of U-velocity profiles along vertical centerline (left) and V-velocity profiles along horizontal centerline (right) for Kn$=0.3989$.

ture point number on the present solver is investigated. As depicted in Fig. 8, the velocity profiles predicted by the present solver with 4×4, 8×8 and 16×16 quadrature points keep the same. But from the enlarged plots, we can find that the results obtained by 4×4 quadrature points slightly deviate from those calculated by 8×8 and 16×16 quadrature points. Therefore, we can conclude that the case with 8×8 quadrature points is fine enough to ensure accurate simulation of flows.

The comparisons of velocity profiles along the horizontal and vertical central lines for Kn$=0.3989$ are demonstrated in Fig. 9. It is within our expectation that the U-velocity profiles obtained by different methods all deviate from the DVM result because of the

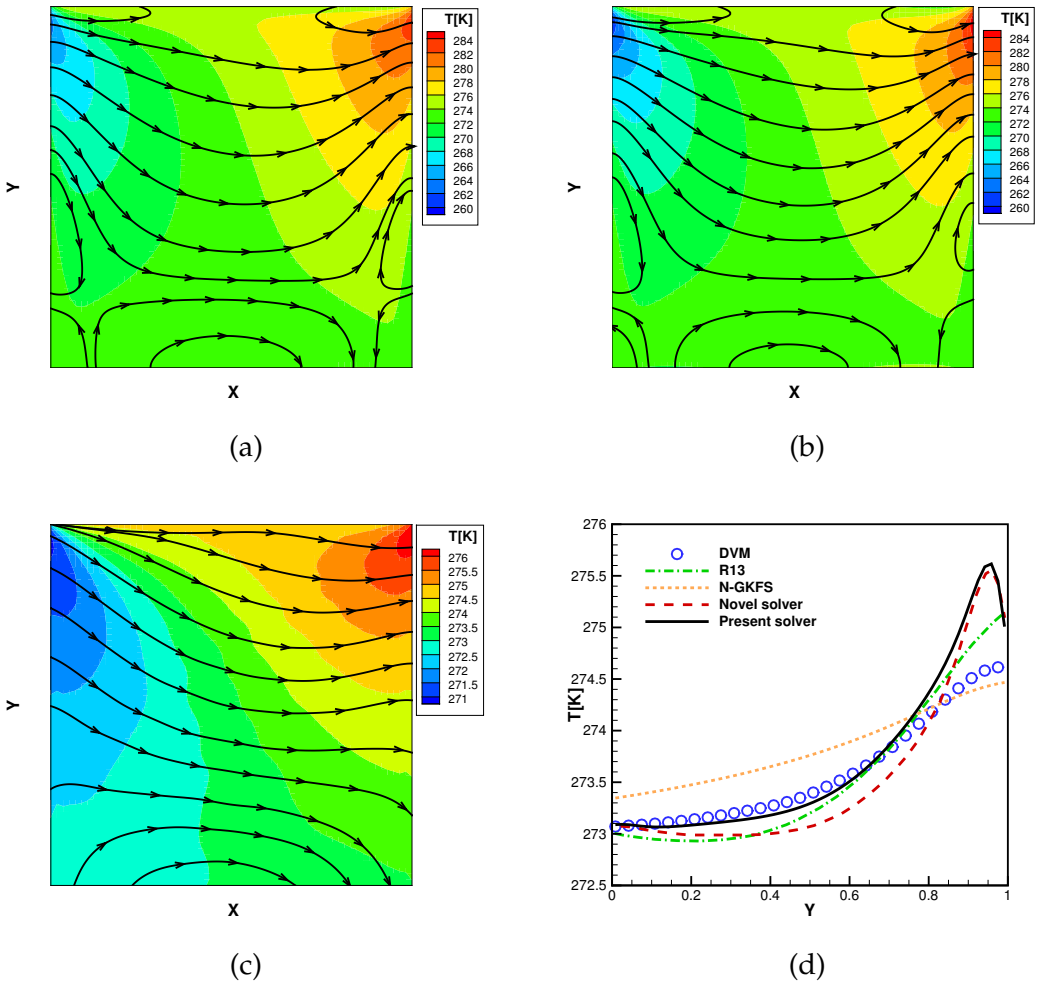

Figure 10: Temperature contours overlaid with heat flux streamlines and profiles for Kn=0.3989: (a) present solver, (b) novel solver, (c) DVM, (d) temperature profiles along vertical central line.

increasing of non-equilibrium effect at Kn=0.3989. But the result of present solver is still in good agreement with the novel solver and is closer to the DVM data than the R-13 equations. The comparison of V-velocity profiles is shown in the right plot of Fig. 9. It is obvious to find that R-13 equations totally over-predict the slip velocity at the wall, while the gas kinetic flux solver under-predicts the slip velocity at the wall. In contrast, the peak value of velocity profile and the slip velocity on the wall predicted by the present solver are in good agreement with the DVM data. In Figs. 10(a), (b) and (c), we compare the temperature contours and the streamlines of heat flux. The heat flux lines predicted by present solver, novel solver and DVM all show the migration from the low-temperature

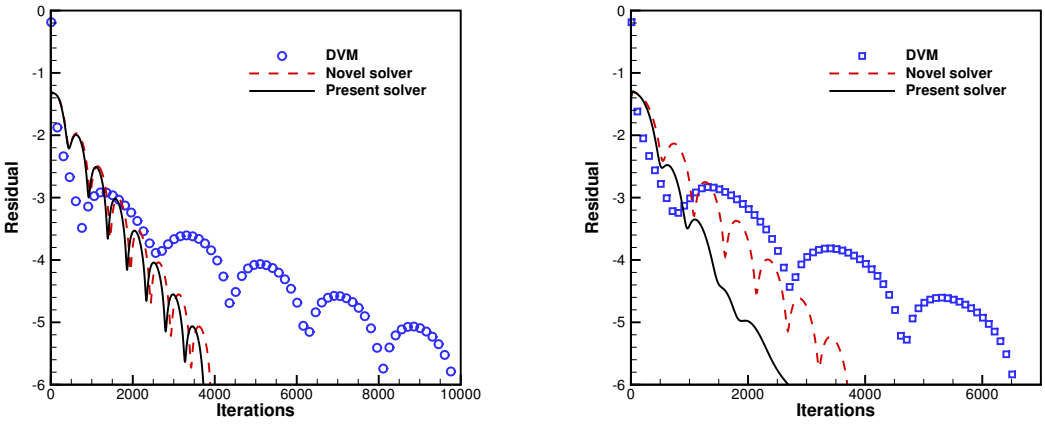

Figure 11: Convergence history for cases of Kn=0.0798 (left) and Kn=0.3989 (right).

region to the high-temperature region. The comparison of temperature profiles along the vertical centerline is presented in Fig. 10(d). In the bottom region of the square cavity, the present solver shows improved results as compared to the novel solver. However, over-prediction of temperature is observed near the moving wall where the non-equilibrium effects are strong [19], which is the limitation of the present solver.

The comparison of convergence histories among the present solver, novel solver, and DVM for Kn=0.0798 and 0.3989 is shown in Fig. 11. The residual is calculated by

$$Residual(\rho)=\sqrt{\sum_{j=1}^{N_y}\sum_{i=1}^{N_x}\left[\boldsymbol{F}_\rho(i,j)\right]^2/\left(N_x\cdot N_y\right)}, \tag{5.9}$$

where $\boldsymbol{F}_\rho(i,j)$ is the numerical flux for density, N_x and N_y are the number of cells in the x- and y-direction, respectively.

The present solver performs much better than the DVM in this aspect, and shows minor improvements as compared to the novel solver.

To validate the accuracy of present solver in the continuum regime, the cases of Reynolds number of Re=100, 400 and 1000 are considered. With the increase of Reynolds number, the computational domain is divided uniformly into 60×60, 80×80 and 100×100 cells, respectively. The reference viscosity μ_0 is related to the Reynolds number and calculated by $\mu_0=\rho_0 U_w L/\mathrm{Re}$. The results from Ghia et al. [40] and N-GKFS [18] are both utilized as the primary benchmark data. Here, we adopt N-GKFS because it can give accurate results in the continuum regime. As shown in Fig. 12, Fig. 13 and Fig. 14, the velocity profiles predicted by the present solver match well with those of Ghia et al. [40] and the N-GKFS. These test cases prove that the present solver can give the accurate results in the continuum regime. It is thus demonstrated that the present gas distribution function

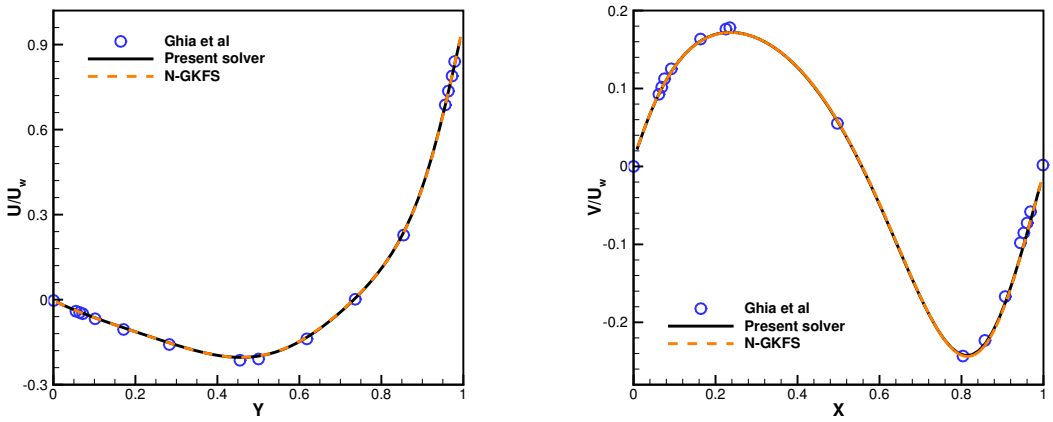

Figure 12: Comparison of U-velocity profiles along vertical centerline (left) and V-velocity profiles along horizontal centerline (right) for Re$=100$.

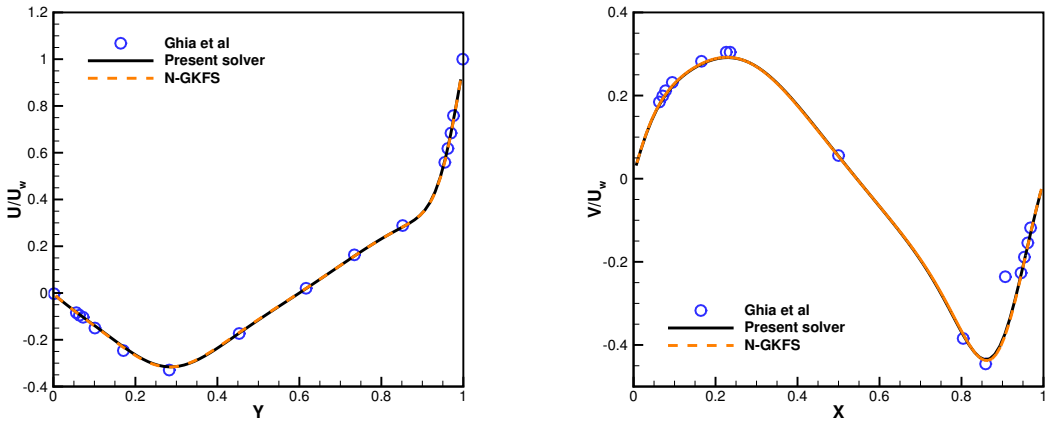

Figure 13: Comparison of U-velocity profiles along vertical centerline (left) and V-velocity profiles along horizontal centerline (right) for Re$=400$.

approximated by the second-order polynomial in terms of $\mathbf{1}$, $\boldsymbol{C}$ and $\boldsymbol{C}^2$ can automatically recover to the first-order CE expansion gas distribution function in the continuum regime.

Table 1 compares the locations of the primary vortex center with different Reynolds numbers obtained by different methods. The maximum relative error between the present solver and those of Ghia et al. [34] is less than 5.86‰, which further validates its accuracy in the continuum regime.

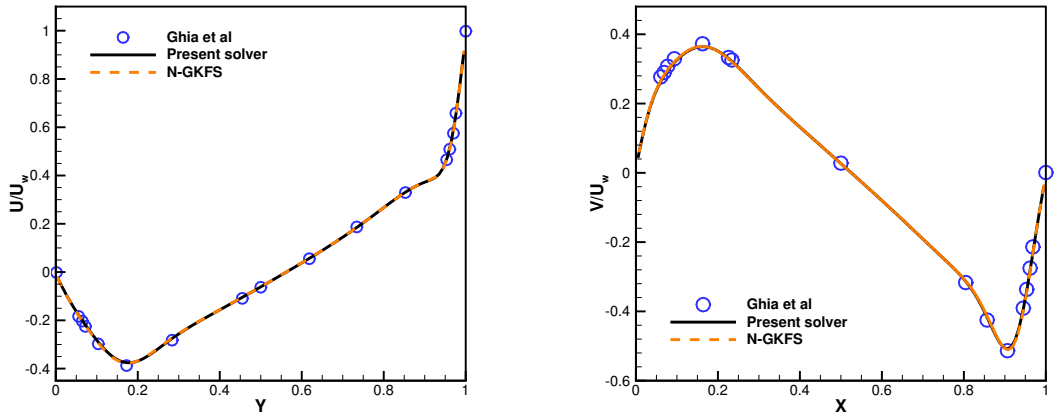

Figure 14: Comparison of U-velocity profiles along vertical centerline (left) and V-velocity profiles along horizontal centerline (right) for Re=1000.

Case 3: Thermal cavity flow induced by temperature gradients at wall.

The third test case is the thermal cavity flow induced by temperature gradients at wall. This test case was once studied by Yang et al. [41] using moment methods. We also adopt the in-house DVM solver to calculate this case as a benchmark to validate the accuracy of present solver. The configuration is shown in Fig. 15. The length of the wall is L. The left and the right walls are maintained at constant temperature of $T_C=263$K. On the top wall and the bottom wall, the temperature is linearly increased from $T_C=263$K to $T_H=283$K in the left half, and then linearly decreased to $T_C=263$K in the right half.

The computational domain for this case is divided uniformly into 60×60 cells. The particle velocity space is discretized by 16×16 quadrature points used by Gauss–Hermite rule for present solver. In this test case, the characteristic length is also chosen as L. Thus, the Knudsen number can also be computed by Eq. (5.5). The mean free path λ is related to the reference viscosity μ_0 and given by

$$\lambda=\frac{4\alpha_0(5-2w_0)(7-2w_0)}{5(\alpha_0+1)(\alpha_0+2)\sqrt{2\pi RT_0}}\frac{\mu_0}{\rho_0}, \tag{5.10}$$

where ρ_0 is the reference density. α_0 and w_0 are parameters of the inter-molecular inter-

Table 1: Locations of primary vortex centers obtained by different methods.

Re	Ghia et al. [40]	N-GKFS	Present GKFS
100	(0.6172,0.7344)	(0.6181,0.7382)	(0.6171,0.7387)
400	(0.5547,0.6055)	(0.5563,0.6056)	(0.5563,0.6061)
1000	(0.5313,0.5625)	(0.5320,0.5653)	(0.5322,0.5658)

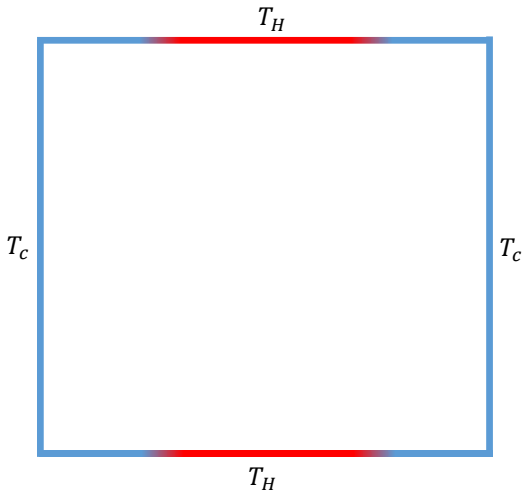

Figure 15: The schematic of thermal cavity flow.

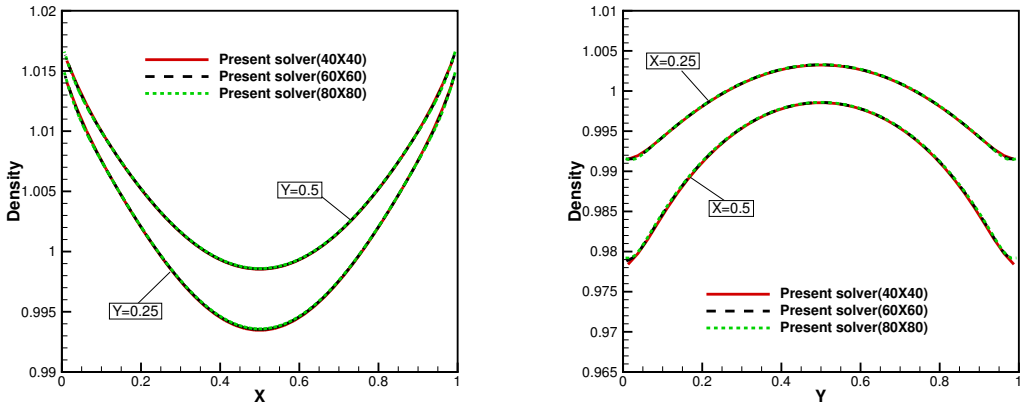

Figure 16: Comparison of density profiles along horizontal line (left) and vertical line (right) with different mesh scales.

action models at the reference state. In this work, the hard sphere model is utilized as reference state, such that $\alpha_0 = 1$ and $w_0 = 0.5$. The viscosity (μ) in the flow field is given by Eq. (5.8) with the viscosity exponent ω equal to 0.81.

A validation of the grid independence for the present solver is conducted by using three sets of mesh scale, including 40×40, 60×60 and 80×80. As illustrated in Fig. 16, the results at the location of $y = 0.25$, $y = 0.5$, $x = 0.25$ and $x = 0.5$ obtained by the mesh scale of 60×60 could converge to the results by 80×80. Thus, 60×60 is fine enough to ensure the accurate simulation.

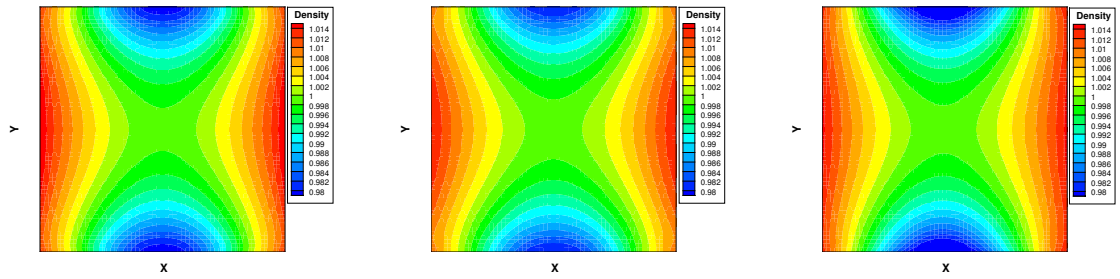

(a) (b) (c)

Figure 17: Density contours for Kn=0.1: (a) present solver, (b) novel solver, (c) DVM.

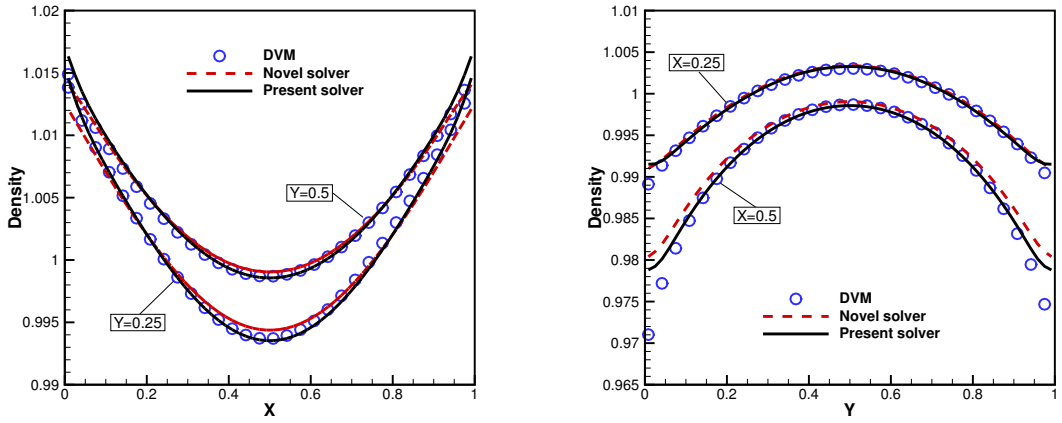

Figure 18: Density profiles along vertical lines (left) and horizontal lines (right).

As shown in Fig. 16, the density contours calculated by the present solver, the novel solver and the DVM are quite similar. For quantitative comparisons, the density profiles along vertical lines and horizontal lines are investigated. As illustrated in Fig. 17, the results predicted by the present solver can match better with the DVM than the novel solver.

As clarified in the Section 3.2, the term $\boldsymbol{C}^2$ in the new distribution function has inherent connections with the energy. And comparing with the distribution function of Grad's 13 moment, the new derived distribution function has the additional moment $\langle \boldsymbol{C}^4 f \rangle$. Thus, it is expected that the present solver will perform better than the novel solver in the prediction of heat fluxes. The comparison of heat flux pattern in the x-direction is shown in Fig. 18. Specifically, Fig. 18(d) gives the quantitative comparison of heat flux at the location of $y=0.25$ and $y=0.5$. It is noted that the heat flux in the x-direction calcu-

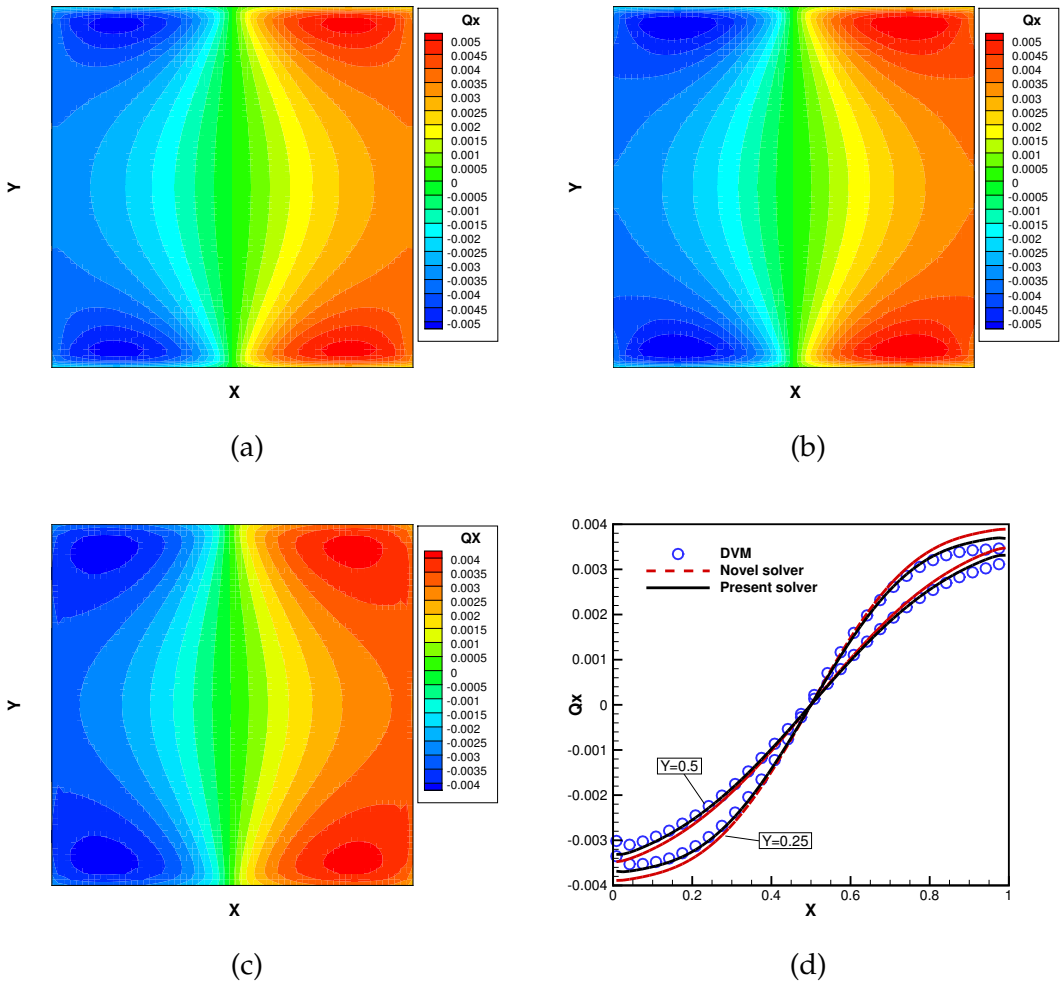

Figure 19: Heat flux contours in the x-direction and profiles for Kn$=0.1$: (a) present solver, (b) novel solver, (c) DVM, (d) profiles along vertical lines.

lated by present solver is closer to that of DVM than the novel solver. The comparison of heat flux in the y-direction is shown in Fig. 19. In comparison with the reference results given by the DVM, the present solver also performs slightly better than the novel solver. We need to clarify that the heat fluxes (including Qx and Qy) in the present solver are obtained by their relationship with coefficients $\tilde{a}_7$ and $\tilde{a}_8$ as follow,

$$Q_x = 5 \cdot \tilde{a}_7 \rho (RT)^3, \quad Q_y = 5 \cdot \tilde{a}_8 \rho (RT)^3. \tag{5.11}$$

Case 4: Pressure-driven Poiseuille flow.

The last case to test the performance of the present solver is the pressure-driven

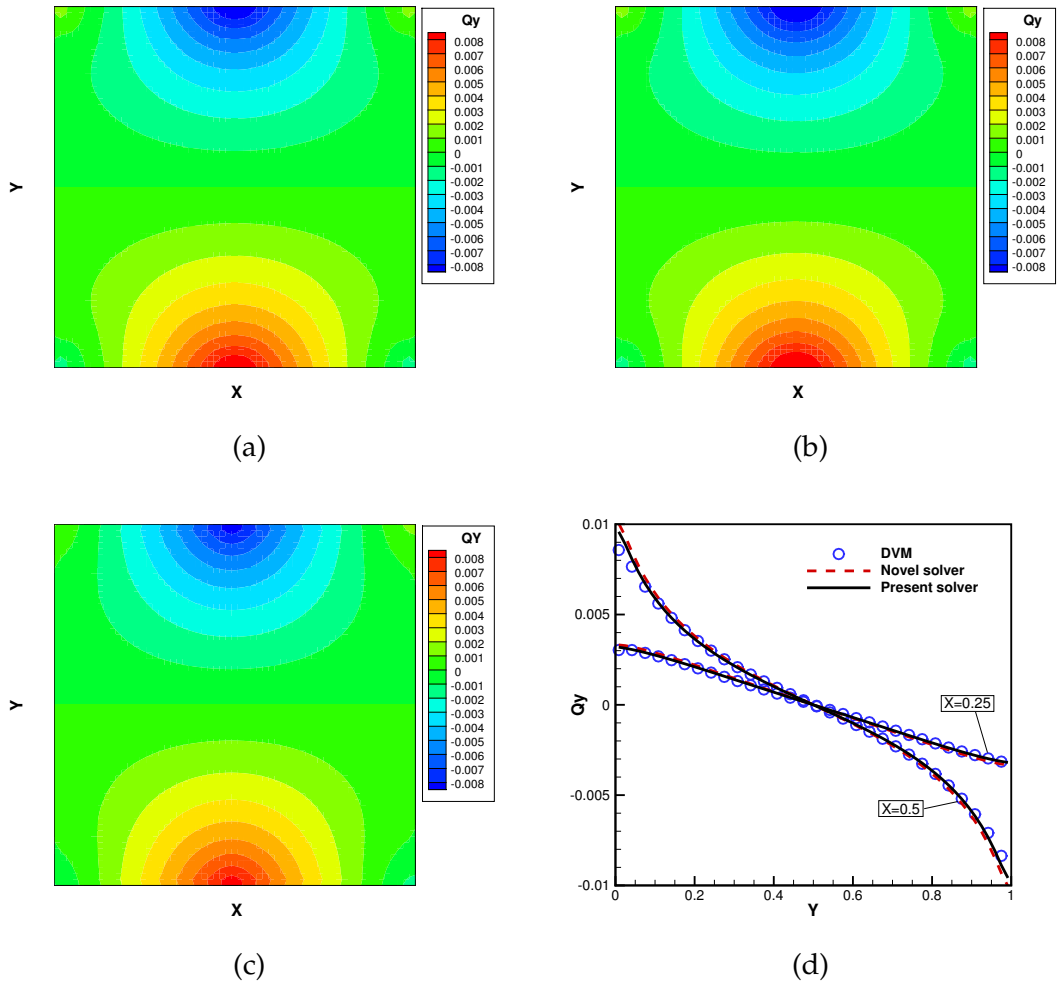

Figure 20: Heat flux contours in the y-direction and profiles for Kn$=0.1$: (a) present solver, (b) novel solver, (c) DVM, (d) profiles along horizontal lines.

Poiseuille flow [42]. As shown in Fig. 20, the aspect ratio is given by $L_x/L_y=3$ and the distance between the upper and the lower walls is $L_y=10\lambda_0$, where λ_0 is the molecular mean free path and will be given later. The reference pressure for this case is $p_0=6.05\times10^{-4}$. The inlet pressure and outlet pressure are set as $p_{in}=3/2p_0$ and $p_{out}=1/2p_0$, respectively.

The gas molecule inside the flow field possesses the diameter of $d=1$ and the mass of $m=1$. The reference density is set as $\rho_0=1.21\times10^{-3}$, with which the mean free path can be calculated by $\lambda_0=m(\sqrt{2}\pi\rho_0 d^2)^{-1}=186$. Then, Knudsen number is determined by Kn$=\lambda_0/L_y=0.1$. In this case, the reference viscosity is computed by $\mu_0=\rho_0\lambda_0U_0/\sqrt{\pi}$ and the real viscosity is determined by Eq. (5.8) with the viscosity exponent equal to 0.5.

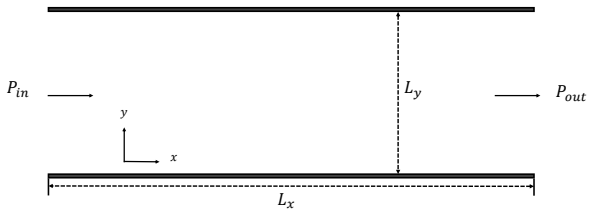

Figure 21: Schematic of pressure-driven Poiseuille flow.

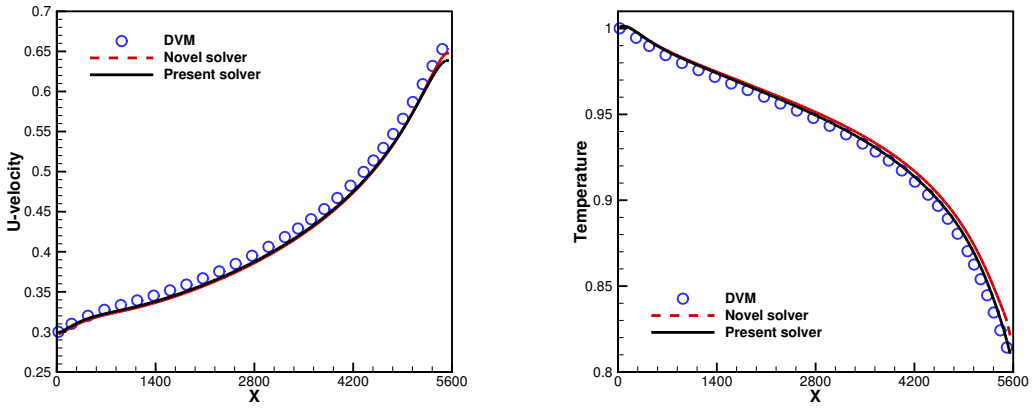

Figure 22: Comparison of U-velocity (left) and Temperature (right) profiles along the horizontal centerline.

The comparison of velocity profiles is shown in the left plot of Fig. 21. Both the present solver and novel solver match well with the DVM data. The right plot of Fig. 21 compares the temperature profiles along the horizontal centerline. The results obtained by the present solver still agree well with that of DVM, whereas the results of the novel solver show clear deviations. The comparison of U-velocity and temperature profiles along the vertical centerline is shown in Fig. 22. We can draw the same conclusion that the present solver can predict the velocity as well as the novel solver, but gives more accurate temperature profile than the novel solver. This may be due to the fact that the moments (especially the term $\langle \boldsymbol{C}^4 f \rangle$) involved in the new distribution function can be closely linked to the energy, thus preforms better than the third-order truncated Hermite polynomial expansion. To analyze the contribution arising from $\langle \boldsymbol{C}^4 f \rangle$, we visualize the coefficient $\tilde{a}_9$ in the flow pattern, which is demonstrated in Fig. 23. Its values along the horizontal and vertical centerline are shown in Fig. 24, which indicate that $\tilde{a}_9$ mainly takes effect in the central region and outlet region. This also interprets the better performance of present solver than novel solver in the prediction of temperature profiles.

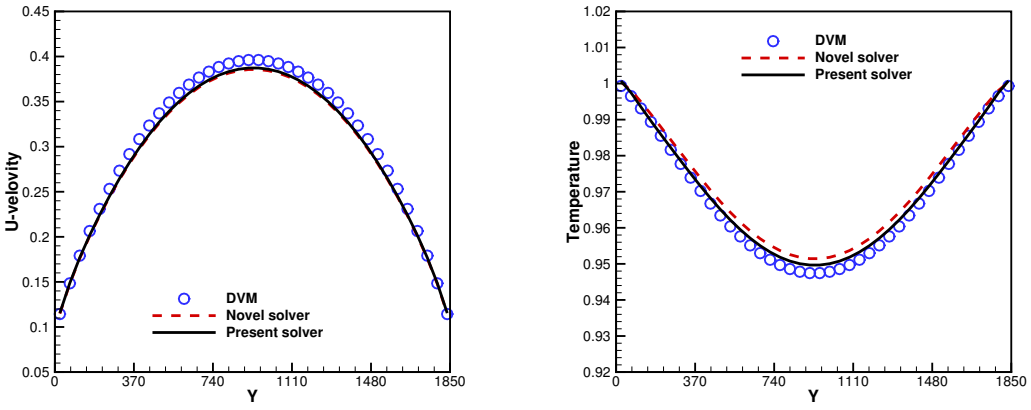

Figure 23: Comparison of U-velocity (left) and Temperature (right) profiles along the vertical centerline.

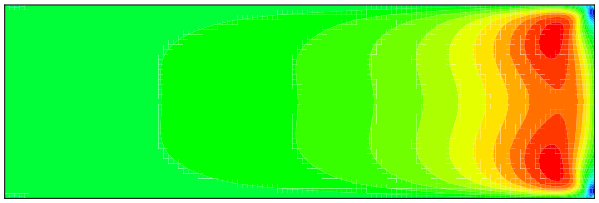

Figure 24: Contour of coefficient $\tilde{a}_9$ in the flow pattern.

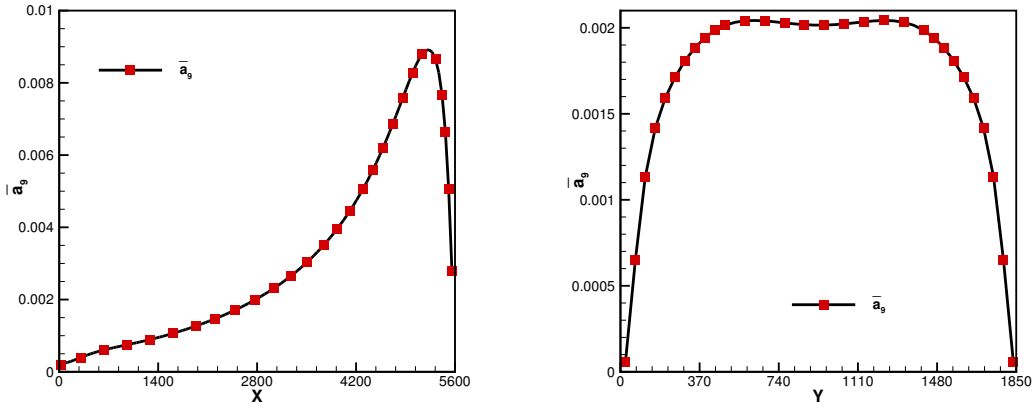

Figure 25: Profiles of coefficient $\tilde{a}_9$ along the horizontal (left) and vertical (right) centerline.

6 Concluding remarks

In this paper, a new gas distribution function is derived based on the second-order polynomial approximation in terms of $\mathbf{1}$, $\boldsymbol{C}$ and $\boldsymbol{C}^2$. Then, a new gas kinetic flux solver based on this distribution function is presented for simulation of flows from continuum regime to transition regime. This solver is established within the framework of FVM and the numerical fluxes at the cell interface are evaluated by the gas distribution function. In addition, an iterative process is employed to calculate the coefficients involved in the distribution function through moment relationships straightforwardly. The numerical validations show that the present scheme can recover the solutions of the NS solver in the continuum regime. In the transition regime, the present solver bears comparable accuracy as the novel solver in resolving the velocity field, but outperforms the latter in the prediction of temperature and heat fluxes.

Acknowledgements

The research is supported by the National Natural Science Foundation of China (No. 12302376), Natural Science Foundation of Jiangsu Province (No. BK20230905), Fundamental Research Funds for the Central Universities (No. 30923011033), National Natural Science Foundation of China (No. 52201329), MOE Tier 1 project at National University of Singapore (A-0005235-01-00).

References

[1] Z. Li, and H. Zhang, *Study on gas kinetic unified algorithm for flows from rarefied transition to continuum,* J. Comput. Phys., 193 (2004), pp. 708–738.
[2] Z. Li, W. Hu, A. Peng, J. Wu, and C. Lee, *Gas-kinetic unified algorithm for plane external force-driven flows covering all flow regimes by modeling of Boltzmann equation,* Int. J. Numer. Meth. Fl., 92 (2020), pp. 922–949.
[3] K. Xu, and J. Huang, *A unified gas-kinetic scheme for continuum and rarefied flows,* J. Comput. Phys., 229 (2010), pp. 7747–7764.
[4] K. Xu, Direct Modeling for Computational Fluid Dynamics: Construction and Application of Unified Gas-Kinetic Schemes, World Scientific, 2015.
[5] Z. Guo, K. Xu, and R. Wang, *Discrete unified gas kinetic scheme for all Knudsen number flows: Low-speed isothermal case,* Phys. Rev. E, 88 (2013), 033305.
[6] Z. Guo, R. Wang, and K. Xu, *Discrete unified gas kinetic scheme for all Knudsen number flows. II. Thermal compressible case,* Phys. Rev. E, 91 (2015), 033313.
[7] Z. Chen, C. Shu, and L. Zhang, *A simplified axisymmetric lattice Boltzmann method for incompressible swirling and rotating flows,* Phys. Fluids, 31 (2019), 023605.
[8] Z. Chen, and C. Shu, *Simplified lattice Boltzmann method for non-Newtonian power-law fluid flows,* Int. J. Numer. Meth. Fl., 92 (2020), pp. 38–54.

[9] Y. LIU, C. SHU, H. ZHANG, AND L. YANG, *A high order least square-based finite difference-finite volume method with lattice Boltzmann flux solver for simulation of incompressible flows on unstructured grids,* J. Comput. Phys., 401 (2020), 109019.
[10] Z. CHEN, C. SHU, Y. WANG, L. YANG, AND D. TAN, *A simplified lattice Boltzmann method without evolution of distribution function,* Adv. Appl. Math. Mech., 9 (2017), pp. 1–22.
[11] Y. WANG, R. DU, AND Z. CHAI, *Lattice Boltzmann model for time-fractional nonlinear wave equations,* Adv. Appl. Math. Mech., 14 (2022), pp. 914–935.
[12] Z. CHEN, C. SHU, AND D. TAN, *High-order simplified thermal lattice Boltzmann method for incompressible thermal flows,* Int. J. Heat Mass. Tran., 127 (2018), pp. 1–16.
[13] L. YANG, C. SHU, W. YANG, AND J. WU, *Simulation of conjugate heat transfer problems by lattice Boltzmann flux solver,* Int. J. Heat Mass. Tran., 137 (2019), pp. 895–907.
[14] K. PRENDERGAST, AND K. XU, *Numerical hydrodynamics from gas-kinetic theory,* J. Comput. Phys., 109 (1993), pp. 53–66.
[15] K. XU, L. MARTINELLI, AND A. JAMESON, *Gas-kinetic finite volume methods, flux-vector splitting, and artificial diffusion,* J. Comput. Phys., 120 (1995), pp. 48–65.
[16] L. YANG, C. SHU, J. WU, N. ZHAO, AND Z. LU, *Circular function-based gas-kinetic scheme for simulation of inviscid compressible flows,* J. Comput. Phys., 255 (2013), pp. 540–557.
[17] Y. LIU, C. SHU, H. ZHANG, L. YANG, AND C. LEE, *An efficient high-order least square-based finite difference-finite volume method for solution of compressible Navier-Stokes equations on unstructured grids,* Comput. Fluids, 222 (2021), 104926.
[18] Z. YUAN, L. YANG, C. SHU, Z. LIU, AND W. LIU, *A novel gas kinetic flux solver for simulation of continuum and slip flows,* Int. J. Numer. Meth. Fl., 93 (2021), pp. 2863–2888.
[19] Z. YUAN, C. SHU, Z. LIU, L. YANG, AND W. LIU, *Variant of gas kinetic flux solver for flows beyond Navier-Stokes level,* Phys. Rev. E, 104 (2021), 055305.
[20] H. GRAD, *On the kinetic theory of rarefied gases,* Commun. Pure Appl. Math., 2 (1949), pp. 331–407.
[21] M. TORRILHON, AND H. STRUCHTRUP, *Regularized 13-moment equations: shock structure calculations and comparison to Burnett models,* J. Fluid. Mech., 513 (2004), 171.
[22] X. GU, AND D. EMERSON, *A high-order moment approach for capturing non-equilibrium phenomena in the transition regime,* J. Fluid. Mech., 636 (2009), pp. 177–216.
[23] Z. LIU, C. SHU, S. CHEN, L. YANG, M. WAN, AND W. LIU, *A novel solver for simulation of flows from continuum regime to rarefied regime at moderate Knudsen number,* J. Comput. Phys., (2020) 109548.
[24] Z. LIU, L. YANG, C. SHU, S. CHEN, M. WAN, W. LIU, AND Z. YUAN, *Explicit formulations of G13-based gas kinetic flux solver (G13-GKFS) for simulation of continuum and rarefied flows,* Phys. Fluids, 33 (2021), 037133.
[25] Z. YUAN, C. SHU, AND Z. LIU, *Grad's distribution functions-based gas kinetic scheme for simulation of flows beyond Navier–Stokes level,* Phys. Fluids, 33 (2021), 122007.
[26] P. BHATNAGAR, E. GROSS, AND M. KROOK, *A model for collision processes in gases. I. Small amplitude processes in charged and neutral one-component systems,* Phys. Rev., 94 (1954), 511.
[27] L. YANG, C. SHU, AND J. WU, *Development and comparative studies of three non-free parameter lattice Boltzmann models for simulation of compressible flows,* Adv. Appl. Math. Mech., 4 (2012), pp. 454–472.
[28] Y. LIU, L. YANG, C. SHU, AND H. ZHANG, *A multi-dimensional shock-capturing limiter for high-order least square-based finite difference-finite volume method on unstructured grids,* Adv. Appl. Math. Mech., 13 (2021), pp. 671–700.
[29] Y. SUN, C. SHU, C. TEO, Y. WANG, AND L. YANG, *Explicit formulations of gas-kinetic flux*

solver for simulation of incompressible and compressible viscous flows, J. Comput. Phys., 300 (2015), pp. 492–519.

[30] Z. YUAN, Z. CHEN, C. SHU, Y. LIU, AND Z. ZHANG, *Construction of non-equilibrium gas distribution functions through expansions in peculiar velocity space,* Adv. Appl. Math. Mech., 15 (2023), pp. 1456–1472.

[31] G. H. GOLUB, AND J. H. WELSCH, *Calculation of Gauss quadrature rules,* Math. Comput., 23 (1969), pp. 221–230.

[32] B. SHIZGAL, *A Gaussian quadrature procedure for use in the solution of the Boltzmann equation and related problems,* J. Comput. Phys., 41 (1981), pp. 309–328.

[33] C. CERCIGNANI, AND M. LAMPIS, *Kinetic models for gas-surface interactions,* Transport Theor. Stat., 1 (1971), pp. 101–114.

[34] W. LIU, Y. LIU, L. YANG, Z. LIU, Z. YUAN, C. SHU, AND C. TEO, *Coupling improved discrete velocity method and G13-based gas kinetic flux solver: a hybrid method and its application for non-equilibrium flows,* Phys. Fluids, 33 (2021), 093309.

[35] L. YANG, C. SHU, J. WU, AND Y. WANG, *Numerical simulation of flows from free molecular regime to continuum regime by a DVM with streaming and collision processes,* J. Comput. Phys., 306 (2016), pp. 291–310.

[36] Z. YUAN, W. ZHAO, Z. JIANG, AND W. CHEN, *Numerical simulation of hypersonic reaction flows with nonlinear coupled constitutive relations,* Aerosp. Sci. Technol., 112 (2021), 106591.

[37] Z. YUAN, Z. JIANG, W. ZHAO, AND W. CHEN, *Multiple temperature model of nonlinear coupled constitutive relations for hypersonic diatomic gas flows,* AIP ADV, 10 (2020), 055023.

[38] A. RANA, M. TORRILHON, AND H. STRUCHTRUP, *A robust numerical method for the R13 equations of rarefied gas dynamics: Application to lid driven cavity,* J. Comput. Phys., 236 (2013), pp. 169–186.

[39] Z. YUAN, W. ZHAO, Z. JIANG, W. CHEN, AND R. AGARWAL, *Modified Nonlinear Coupled Constitutive Relations Model for Hypersonic Nonequilibrium Flows,* J. Thermophys. Heat Tr., 34 (2020), pp. 848–859.

[40] U. GHIA, K. GHIA, AND C. SHIN, *High-Re solutions for incompressible flow using the Navier-Stokes equations and a multigrid method,* J. Comput. Phys., 48 (1982), pp. 387–411.

[41] W. YANG, X. GU, D. EMERSON, Y. ZHANG, AND S. TANG, *Modelling thermally induced non-equilibrium gas flows by coupling kinetic and extended thermodynamic methods,* Entropy, 21 (2019), 816.

[42] Y. ZHENG, A. GARCIA, AND B. ALDER, *Comparison of kinetic theory and hydrodynamics for Poiseuille flow,* J. Stat. Phys., 109 (2002), pp. 495–505.